Fachhochschule Wiener Neustadt
> Technische Studiengänge

2. Bachelorarbeit

Application of Microwave Methods for Characterization of NEG Coatings and Obstacle Detection in Accelerator Beam-pipes

FH-Bachelorstudiengang
Mechatronik / Mikrosystemtechnik

Mechatronik-Autonomes Fahrzeug

Name: David Seebacher
Matrikelnummer: 0620274033

FH-Betreuer: Prof.(FH) DI Frais-Kölbl
Datum: 31.5.2009

Fachhochschule Wiener Neustadt
> Technische Studiengänge

Titel der Bachelorarbeit:

Application of Microwave Methods for Characterization of NEG Coatings and Obstacle Detection in Accelerator Beam-pipes

2. Bachelorarbeit

Eingereicht von: David Seebacher

am: **Fachhochschul-Bachelorstudiengang Mechatronik / Mikrosystemtechnik**

Vertiefung: Mechatronik-Autonomes Fahrzeug

Begutachter: Prof.(FH) DI Helmut Frais-Kölbl

Wiener Neustadt: 31.5.2009

_____

Ich versichere,

dass ich die Bachelorarbeit selbständig verfasst, andere als die angegebenen Quellen und Hilfsmittel nicht benutzt und mich auch sonst keiner unerlaubten Hilfe bedient habe und diese Bachelorarbeit bisher weder im In- noch im Ausland in irgendeiner Form als Prüfungsarbeit vorgelegt habe. Die von mir eingereichte schriftliche Version stimmt mit der digitalen Version der Arbeit überein.

_____ Datum

_____ Unterschrift

Kurzzusammenfassung:
In vielen Teilchenbeschleunigern, unter anderem im LHC der Europäischen Organisation für Kernforschung CERN, werden NEG Beschichtungen eingesetzt. In manchen Beschleunigern hat es Hinweise auf einen relevanten Einfluss der Beschichtungen auf die Beam coupling Impedanz gegeben, es existieren dazu jedoch teils widersprüchliche Aussagen. Daher wurden in dieser Arbeit die elektromagentischen Eigenschaften von NEG Beschichtungen mittels Hohlraum-Resonator-Verfahren bestimmt.
Der zweite Teil dieser Arbeit beschäftigt sich mit einem Mikrowellen–Hohlleiter-Reflektometer, welches am CERN vor einigen Jahren entwickelt wurde und zur Qualitätskontrolle während des Baus und Reperatur des LHC verwendet wurde. Um den einwandfreien Betrieb zu gewährleisten und teure Eingriffe zu vermeiden, wird Mikrowellen-Hohlleiter-Reflektometrie im Beam-Screen angewandt, um Störobjekte aufzuspüren. Es wurden bislang einige Objekte gefunden, jedoch existieren weder Messwerte über Einfluss von Größe und Orientierung verschiedenen Störkörper noch sind die genauen Grenzen des des Systems bekannt.

Schlagwörter:
Non Evaporable Getter NEG, Hohlraum-Resonator-Verfahren, Mikrowellen-Hohlleiter-Reflektometer

Abstract:
In many particle accelerators, including the LHC at the European Organization for Nuclear Research CERN, NEG coatings are used to improve vacuum performance. In other particle accelerators there have been hints that those coatings could have a relevant impact on the beam coupling impedance, however the data available is contradictory. To clarify the possible impact of NEG coatings the electromagnetic properties have been measured. The measurements have been carried out by means of cavity perturbation method.
The second part of this thesis deals with the microwave waveguide reflectometer developed at CERN several years ago, which is used as part of the quality assurance test program for the LHC assembly. To ensure optimum operation and to avoid an expensive removal of any foreign object from inside the LHC beam-screen after its completion, microwave reflectometry is performed. Until now several objects have been found by means of reflectometry, but so far neither precise data about the reflections of different foreign objects, nor the precise limits of the system are known.

Keywords:
NEG, cavity perturbation method, microwave waveguide reflectometry

Table of Contents

1 Introduction

1.1 CERN

The European Organization for Nuclear Research (CERN) was founded in 1954. The name comes from the French abbreviation of *Conseil Européen pour la Recherche Nucléaire* CERN, which was a provisional council established by 11 governments in 1952 to set up the laboratory. Today CERN has 20 member states and collaborates with many non-member states all over the world. CERN is also known as the largest particle physics laboratory in the world and famous for its accelerators. The main site of the laboratory is located in Meyrin, a small village near Geneva, close to the French border and parts of its complex are on French territory.

Currently one of the important focuses is on the repair of the Large Hadron Collider LHC which got operational in autumn 2008 and is capable of accelerating electrons to energies up to 7TeV. The LHC has to be repaired after a fault of one of the superconducting magnets interconnections soon after its completion. The reconstruction of the LHC is scheduled to finish in July 2009 and it will again be put into operation in September 2009.

Beside particle physics, there are many spin-offs into other technologies, with the World Wide Web, developed in 1990/91 at CERN, being the one of most famous.

1.2 LHC

The LHC is the largest and highest-energy synchrotron particle accelerator in the world. There are two adjacent beam pipes, in which the beams circulate in opposite directions. Each particle beam can be accelerated to a maximum of 7TeV, providing collisions at energy up to 14TeV. The LHC has been installed in the tunnel constructed previously for the LEP, about 100m below surface with a circumference of 26.65km and a diameter of 8.48km. In Figure 1.1 an aerial picture of the LHC site, taken above Geneva in the direction of the Jura is shown. The main site of CERN is located outside the small village Meyrin, near the ATLAS experiment, in the left part

of the picture. All in all there are four intersections where the beams can be brought into collisions. The four detectors ATLAS, CMS, ALICE and LHCb are located at these intersections.

Figure 1.1 Aerophoto of LHC[1]

In order to achieve the high magnetic fields needed to steer the particle beams, in the confines of the underground tunnel and to have reasonable operating costs, most of LHC's magnets are superconducting. This includes 1232 dipole magnets and 392 quadrupole magnets, comprising the main ring. The superconducting cables and coils of these magnets operate at a temperature of 1.9K, this requires about 96t of super-fluid helium to cool the magnets, making the LHC the biggest cryogenic facility in the world.

In Figure 1.2 the standard cross-section of a dipole magnet is shown. The two beam pipes surrounded by the windings of the two coils can be seen in the center. Installed inside the beam pipes there is the beam-screen that will be described later. The windings and the iron yoke around them are cooled down to 1.9K, forming the so called cold mass, which includes various supply lines and the bus bars for the quadrupoles, they also have to be cooled as they are superconducting too. To improve the thermal insulation, a thermal shield, kept at around 55 to 75K, is placed between the cold bore (1.9K) and the outer vacuum vessel (room temperature).

[1] Source: http://startswithabang.com/wp-content/uploads/2008/05/lhc-sim.jpg, 26. 2. 2009

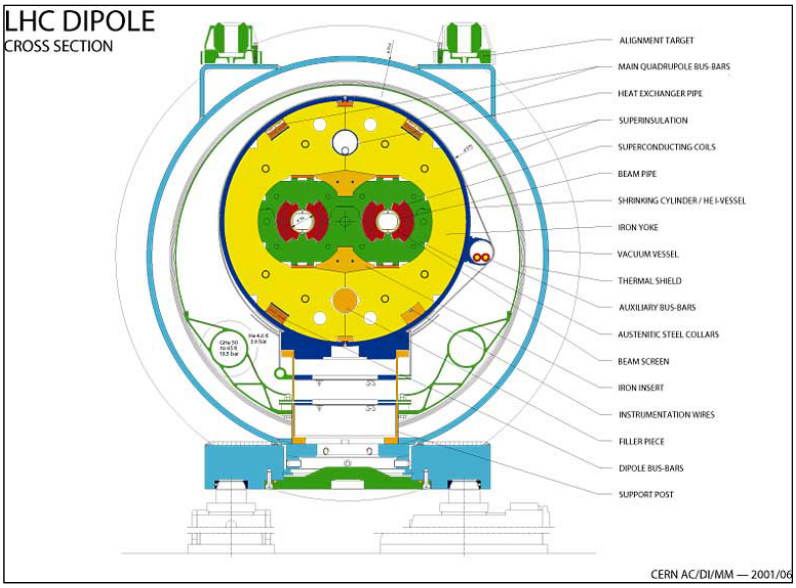

Figure 1.2 Standard cross section dipole magnet[2]

1.3 Motivation for the Determination of Electromagnetic Properties of NEG and Carbon Coatings

Non Evaporable Getter (NEG) is a metallic alloy used to improve certain properties of particle accelerators, in Chapter 3.2 there is a more detailed description. NEG coatings have been applied in different synchrotrons, nevertheless there are inconsistent statements about the influence of NEG coating on the machines impedance. At the synchrotron radiation facility ELLETRA (Trieste, Italy) an increase of the transverse impedance has been measured after each installation of a NEG vacuum chamber [1][2].

In order to understand the effects observed at ELLETRA, specialists at the Synchrotron SOLEIL (Gif-sur-Yvette, France) tried to simulate the effect of the NEG-coating. Their results were in qualitative, but not in quantitative agreement with the measurements done at ELLETRA [3][4].

At the European Synchrotron Radiation Facility ESRF NEG coatings are used as well and there they did not observe any impact on the impedance of the machine [5].

[2]Source: http://cdsweb.cern.ch/record/843195/, 15. 5. 2009

As a big increase in the imaginary part of the impedance was observed at ELLETRA and since thin metallic layers can show a capacitive behavior at high frequencies, described in chapter 3.1, there was the suspicion that NEG could show such a behavior. If this was true, some of the observed effects could be explained easily. Therefore a measurement of the dielectric constant, at the maximum frequency range of interest (around 3 GHz) for the Super Proton Synchrotron (SPS) was proposed. To perform these measurements the cavity perturbation method, described in chapter 3, was used. If the coatings are purely conductive at those frequencies they should behave like a bad conductor on a good one, so barely visible comparable to a dirty surface[6].

As carbon coatings are used as well, and they can show similar behavior, they have also been tested to ensure that they do not have any impact on the impedance.

1.4 Microwave Reflectometry on the Beam Pipe

For the optimum operation of the LHC, it is of the utmost importance that the beam-screen is perfectly prismatic, clean and free of any obstacles larger than the size of a pinhead. During the manufacturing and installation procedure however, there is a non-negligible risk of permanent deformation or that a foreign object is left inside. Due to the fact that the superconducting LHC magnets are working at cryogenic temperatures, they are very sensitive to energy deposition leading to temperature rises and therefore the beam hitting a very small object (0.1mm thickness) can already cause a particle shower entering a magnet sufficient to make it to quench. Even if only one magnet quenches, the whole system has to shut down, the magnet has then to be cooled down again. This costs time and money and in the case that an obstacle has to be removed after the completion of the LHC installation, it takes considerably more time and effort to get even the tiniest obstacle out of the beam screen. The magnets have to be warmed up, the vacuum broken, and at least one of the interconnections opened to provide access and vice versa after the removal.

In addition, after some operational time with beam, a certain time for cooling will need to be allocated until the radiation is below acceptable limits. So even a small nut, forgotten inside the

beam-screen is capable of causing a shutdown of the LHC for a long period. This is very costly and hence should be avoided under all circumstances.

As part of the quality assurance test program, different methods to detect obstacles are used. One of these is waveguide mode Time Domain Reflectometry, which works with RF-waves and therefore there is no need to insert any measurement tools into the beam-screen. The big advantage is that the actual state of the beam-screen isn't influenced by the measurement which gives a rapid assessment about the state of the beam-screen. Additionally the measurement isn't as much restricted in range as for example with an Endoscope, which is limited by the length of the control cable. The data measured can be stored easily and kept for later analysis and comparison.

The reflections caused by objects depend on their electromagnetic properties. To ensure, that objects that aren't detectable by means of microwave reflectometry, are still found, additional visual inspection and endoscopy is performed, both on the surface and in the tunnel. As detection is very dependent on the obstacle's properties, two different wave modes are used to perform the reflectometry, to gain as much information as possible.

1.5 Motivation for Characterization of Objects

So far a handful of objects have been found by means of Beam-screen Reflectometry, but precise characterization of which objects cause which reflections and a determination where the limits of the detector are has not been done yet. The reflections depend on many different parameters, like size volume, shape, electromagnetic properties and orientation. Hence it is rather difficult to determine from a particular reflection which obstacle there is and if it can present a serious danger for the LHC. Another reason for doing these characterization tests is to provide new users with a quick overview and first impression about the abilities and limits of the system and to enable them to interpret traces and gain some experience without the need to do further tests. This is rather important, as at the moment only a handful of people know how to operate the system and have experience in interpreting the data. So for future use or in case of unavailability of the current operators, the results of the characterization tests can provide a

rapid comparison and allows new users to more reliably come to conclusions about an obstacle from the reflections obtained.

2 Measurement Equipment

2.1 S Parameters

Scattering or S-parameters are used to describe the behavior of a linear electrical network in the frequency domain. Although S-parameters can be applied from DC up to any frequency, they are usually used in radio frequency (RF) and microwave engineering. At these high frequencies it is more convenient to describe a given network in terms of waves rather than voltages and currents.

In microwave engineering, networks are not described anymore in terms of poles, but rather in terms of ports. A port consists of 2 poles, so a 4 pole network would be a 2 port one, as the simple network shown in Figure 2.1. In case of a 3 pole network, for example a simple voltage divider, one of the poles can be seen as a common connector and is linked to both of the 2 ports that are assigned to that network.

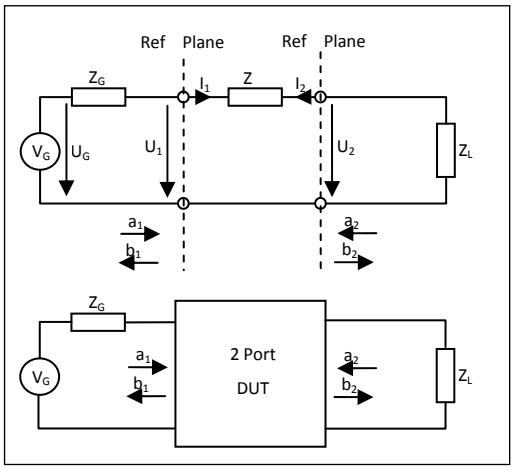

Figure 2.1 4-pole 2-port network [7]

In the upper part of Figure 2.1 a simple 4 pole network is shown with the corresponding voltages and currents, a_n represents the waves travelling towards port n and b_n represents the

waves going away from port n. The parameters a_n and b_n are normalized to the system's impedance Z_0, usually 50Ω and have the unit $\sqrt{power}$. They are linked to the voltages and currents as follows:

$$a_1 = \frac{U_G}{2 * \sqrt{Z_0}} = \frac{voltage\ \ towards\ port1}{\sqrt{Z_0}} = \frac{U_1^i}{\sqrt{Z_0}} \tag{2.1}$$

$$b_1 = \frac{U_1'}{\sqrt{Z_0}} = \frac{reflected\ voltage\ port1}{\sqrt{Z_0}} \tag{2.2}$$

So a_1 is the wave going into the device at port 1 and b_1 is the wave coming out of port 1. As the parameters are normalized to the impedance they can also be calculated by the current according to Ohm's law.

$$a_1 = \frac{U_1^i}{\sqrt{Z_0}} = I_1^i * \sqrt{Z_0} \tag{2.3}$$

Furthermore the power going into port 1 can be calculated as follows:

$$P_1^i = \frac{1}{2} * |a_1|^2 = \frac{\left|U_1^i\right|^2}{2 * Z_0} = \frac{\left|I_1^i\right|^2}{2} * Z_0 \tag{2.4}$$

The same formula is valid for the reflected power. The voltage and current values are given with their peak values and the division by 2 is the result of the conversion to RMS values.

The relationship between a_n and b_n parameters can be expressed by a set of linear equations. The following equation shows calculations for a 2 port network.

$$\begin{aligned} b_1 &= a_1 * S_{11} + a_2 * S_{12} \\ b_2 &= a_1 * S_{21} + a_2 * S_{22} \end{aligned} \tag{2.5}$$

The S stands for scattering parameters, S_{11} expresses the reflection at port 1 and S_{12} expresses the transmission from port 2 to port 1. To measure the S-parameters each port has to be matched with its correspondent impedance. These equations can be expressed in matrix form as shown below.

$$\begin{pmatrix} b_1 \\ b_2 \end{pmatrix} = \begin{pmatrix} S_{11} & S_{12} \\ S_{21} & S_{22} \end{pmatrix} * \begin{pmatrix} a_1 \\ a_2 \end{pmatrix} \tag{2.6}$$

The matrix above can be written in a general way for an n-port as **B**= **S***A. Both matrixes A and B have the size n*1. The scattering matrix S has to have the dimension n*n, furthermore the number of S-parameters grows with n^2, where n is the number of ports.

In Figure 2.2 the scattering parameters and their relationships are shown. Every S-parameter has two indexes S_{mn}, the first one, m, refers to the measurement point and the second one, n, to origin of the signal. The indexes represent the number of the port.

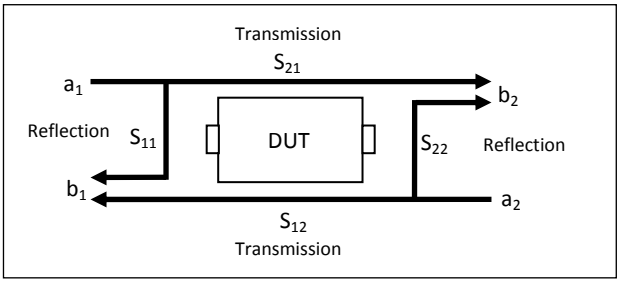

Figure 2.2 Scattering parameters [7]

To derive the S-parameters the transmitted and received signals have to be compared, the S_{11} parameter for example can be derived from $S_{11} = \frac{b_1}{a_1}$.

For passive components the S-parameters can't exceed 1, as that would be equal to an increase in power. Most of the passive networks are reciprocal, that means the transmission and reflection from two ports is the same for both directions, while for an amplifier or a circulator this is not the case and therefore these devices are non-reciprocal. For the measurements of S-parameters a network analyzer as described in chapter 2.2 is used.

2.2 Network Analyzer

2.2.1 General

A network analyzer is the primary instrument for characterizing radiofrequency and microwave systems. The results of a measurement with a network analyzer are the scattering parameters of the measured circuit.

The basic working principle is to send a sine wave of a certain frequency into the network of interest, also called Device Under Test (DUT), and to measure the properties of the transmitted and/or reflected wave. As the scattering parameters of one frequency are not very meaningful, this is done over a frequency range of interest and a plot of the scattering parameters in dependency of frequency is obtained.

There are mainly two different kinds of network analyzers, scalar and vector. Scalar analyzers (SNA) only measure the amplitude and not the phase, vector network analyzer (VNA) do both. Nowadays only vector network analyzers are used, so the word network analyzer usually already refers to a vector network analyzer.

A network analyzer can further more be categorized through the number of ports available. Basic network analyzers have two ports, but for complex networks it can be useful to have more ports available in order to allow easier and faster measurements.

For example to measure a circulator it is much more convenient to do that with a network analyzer with at least 3 ports, otherwise it would be necessary to do 3 different measurements to obtain the whole scattering matrix(3x3), with the need to change the cables between the measurements. It not only takes more time to use a 2 port network analyzer, it also produces redundant data of the reflection scattering parameters. So the advantage of a network analyzer able to cope with the number of ports of the network to be analyzed is obvious.

2.2.2 Mixer

A network analyzer operates with the same working principle as a superheterodyne receiver. As there is only one frequency of interest at a given moment, there is the need to filter the signal, and as it is difficult to built a narrow band adjustable filter for high frequencies, the signal is converted to a lower frequency and then filtered. Figure 2.3 shows the basic elements of a superheterodyne receiver. The signal from the aerial is amplified and then mixed with the signal from the local oscillator. The results are two signals with the frequencies of the two input signals added and subtracted, RF+LO and RF-LO, if the local oscillator's frequency is lower than the RF frequency. So there are two signals after the mixer, as the sum has an even higher frequency

than the original one, the difference signal is used. Furthermore the intermediate frequency (IF) is determined by IF = RF-LO, hence the IF filter is tuned to this frequency. But it is even more convenient to tune the local oscillator than to tune the frequency of the filter. So the IF is held at a constant frequency and to adjust it to the frequency of interest, the local oscillator is tuned to LO=RF-IF.

The signal after the IF-filter is then amplified, demodulated and finally amplified again for the speakers.

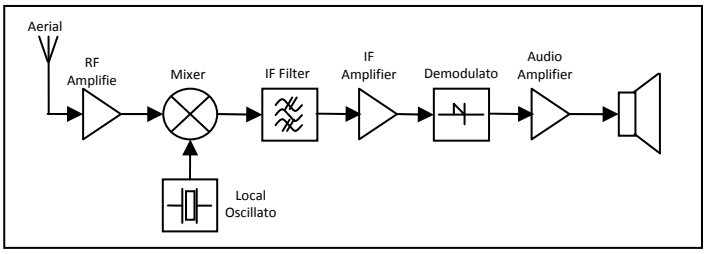

Figure 2.3 Superheterodyne receiver [7]

The ideal mixer can be mathematically described as follows. The two input signals from RF and LO are sine waves.

$$S_{RF}(t) = A_{RF}(t) * \cos(2\pi f_{RF} * t)$$
$$S_{LO}(t) = 2 * \cos(2\pi f_{LO} * t) \quad (2.7)$$

The output signal can be described as a multiplication of the two input signals.

$$S_{IF}(t) = S_{RF}(t) * S_{LO}(t) = 2 * A_{RF}(t) * \cos(2\pi f_{RF} * t) * \cos(2\pi f_{LO} * t) \quad (2.8)$$

After applying the addition theorem the result is:

$$S_{IF}(t) = A_{RF}(t) * \cos(2\pi(f_{RF} + f_{LO}) * t) + A_{RF}(t) * \cos(2\pi(f_{RF} - f_{LO}) * t) \quad (2.9)$$

And as the IF filter is tuned to f_{RF}-f_{LO} the ideal output signal can be described as:

$$S_{IF}(t) = A_{RF}(t) * \cos(2\pi f_{IF} * t) \quad (2.10)$$

One of the important properties of the mixer is that the information in amplitude and phase doesn't change. The signal is only transferred to another lower frequency which is easier to handle.

Summing up, by tuning the LO we are able to select which input frequency is being converted to the IF and the signal passing through the IF-filter is then the one of interest. We obtain a signal with the same information (phase and amplitude) as the input signal gives us but at a lower frequency.

2.2.3 Working Principle

A description of the working principle is shown in the block diagram in Figure 2.4. In the upper left corner the variable sine or carrier wave (CW) generator can be seen. The sine wave generator is followed by a variable attenuator and a selector switch for the direction of propagation. So the frequency, amplitude and direction of propagation through the DUT can be adjusted. This part of the network analyzer represents the signal generator mentioned above.

The signal is transferred to the DUT via directive couplers on each port. These directive couplers extract a portion of the forward and backward travelling wave. Each output port only extracts the signal of the corresponding direction. The upper port of the directive coupler in the diagram extracts only a portion of the forward travelling direction and the lower port only from the backward travelling signal. So the directive coupler is used to separate the forward (transmission) and backward travelling (reflection) wave from the DUT.

The Mixer stage mixes the signal from the directive couplers, which is usually in the range of GHz, with help of the Reference Oscillator, down to the IF of a few MHz. The Mixer is followed by a band pass filter, exactly tuned to the IF. The signal passing through the Mixer is just changed in frequency amplitude but phase information isn't affected. This is a very important characteristic of the mixing process.

As the IF is fixed we have to adjust the frequency of the Reference Oscillator to be able to measure the frequency of interest. This change of the Reference Frequency is done as described above synchronously to the change of the sine wave generator. In reality these two frequencies are obtained by frequency multipliers and other sophisticated circuits fed by the same oscillator. The frequency of the CW signal and the reference signal is shifted by exactly the IF in order to have a fixed frequency after the mixer.

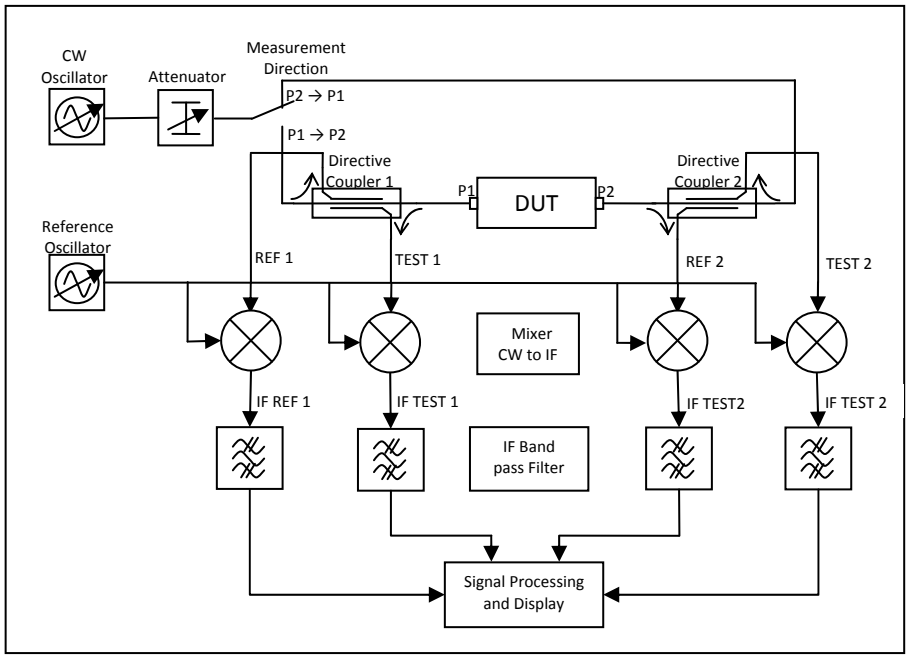

Figure 2.4 Block diagram network analyzer [26]

After the IF band pass filters the signal arrives at the signal processing, where it is sampled. The band pass filters are also digital nowadays, so the sampling is actually done before the filters. The signals now contain information of amplitude and phase. In order to obtain the scattering parameters the signals TEST1 and TEST2 have to be compared with one of the reference signals REF1 or REF2, depending on the direction of the measurement. The reference signal has the same attributes as the wave sent into the DUT and the test signals contain information about the transmitted and reflected waves. To determine for example the S_{11}-parameter the measurement signal is generated at port 1 and the TEST1-signal has to be compared with the REF1-signal.

Through comparing the two signals, the measurement is independent of the amplitude of the CW-signal, as long as the device is linear. The above described process is done at a certain CW-frequency of interest and repeated for different frequencies, according to the range and number of points set.

2.2.4 Accuracy

The accuracy of a network analyzer is limited by different parameters, as for example by the dynamic range, the number of measurement points and the bandwidth of the Intermediate Frequency filter. The dynamic range is given by the ADC and the noise level at a certain frequency. The number of points and the bandwidth of the IF-filter are usually adjustable for modern instruments. For modern VNAs the maximum number of points is 16001 and the narrowest bandwidth is as low as 1 Hz, these two parameters influence the measurement time. The narrower the bandwidth is set, the longer transient effects are an issue and the longer one frequency has to remain at the input. Furthermore the sweep time has to be larger for a narrower bandwidth. A narrow bandwidth has the advantage of a very precise measurement due to less noise, with the disadvantage of a long measurement time. The higher the numbers of points, the more measurements at different frequencies are performed. So a reasonable compromise has always to be made between measurement time and precision.

2.2.5 Calibration

To increase precision and exclude all systematic errors calibration can be used. Systematic errors are cable attenuation, phase shifts (electrical delays), finite directivity of the directive couplers, source and load mismatches inside the instrument and on cables or other devices, such as amplifiers, between the network analyzer and the DUT. As all these parameters are frequency dependent, the system has to be recalibrated for every change of the frequency range. The calibration is done at the connections to the DUT, to remove all errors as far as possible.

The calibration requires the measurement of 3 well defined standards, usually open, short and load, but in general there just have to be well known differences in amplitude and phase. As for waveguides, it is very difficult to match them properly, 2 shorts with different phase (location) and open, are the standards most commonly used. Once the calibration is done all errors inside the instrument up to the DUT are removed numerically, so the measured quantities are those of the DUT.

If the calibration is done at the end of a line, as for example a transistor on a PCB, the smith chart can be used in reflection mode to determine whether the line is terminated properly. With the help of the smith chart the values for a matching circuit can be obtained easily.

2.3 Waveguides

2.3.1 General

A waveguide is a structure capable to guide electromagnetic waves. Imagine an electromagnetic wave propagating in free space with the difference that the wave is reflected at the conductive surface of the waveguide, the wave now propagates along the axis of the waveguide. Waveguides are used for both signal and power transmission. For the later, they are well suited, as they have small losses restricted to the losses of the induced wall currents, which are low for a good conductor such as copper. Waveguides are usually used in microwaves and in radar applications. The most common used waveguide is a waveguide with a rectangular cross section, but also waveguides with a round cross section are used. They have the advantage of the possibility to build rotating joints, necessary for radar antennas, as they are rotating around their axis.

2.3.2 Modes

At the walls of the waveguide there can't be a parallel electric field due to the conducting surface, so there can't be any TEM (Transversal Electro Magnetic) waves in waveguides. This limits the field patterns in waveguides. Basically they are differentiated between TM- (transversal magnetic) or E- (E-field in direction of propagation) modes and TE- (transversal electric) or H- (H field in the direction of propagation). Below the cutoff frequency of a mode, waves of that mode are not able to propagate, as the wavelength is bigger than the space available. The modes can be furthermore categorized by two indexes H_{mn} and E_{mn}. The first index *m* describes the number of half waves in the horizontal and the second index *n* in the vertical direction. In Figure 2.5 the vertical electric field of the first 3 H-modes over the horizontal plane, normalized to the maximum values of the electric field and the waveguide dimensions, is plotted. The blue line shows the pattern of the H_{10}-mode, where one half wave

fits into the waveguide. The green line represents the pattern of the H_{20}-mode and the red the H_{30}-mode, with 2 and 3 half waves respectively in the horizontal plane.

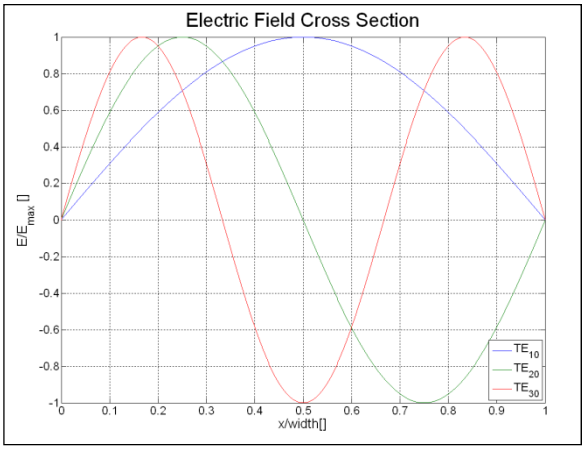

Figure 2.5 Standing waves

The cutoff frequency depends on the geometry of the waveguide. For a rectangular waveguide with a greater width than height, the first mode will be H_{10}, with a cut off frequency of $f_c = \frac{v}{2*width}$. This is due to the fact that half of the wavelength has to fit into the cross section, in order to be a standing wave. The formula can be derived by $v = \lambda_c * f_c$ and $\lambda_c = 2 * width$. For the H_{10} mode the distribution of the vertical electric field follows a sine wave in the horizontal plane. The higher the frequency gets, the more half waves fit into the waveguide. The H_{20} has the doubled cutoff frequency of the H_{10} mode as two half waves have to fit into the waveguide. The H_{20} sets the upper frequency limit, where only a single mode, the H_{10}, is able to propagate. This is only true if the waveguide height is less than half its width, in the case of the cutoff frequency of the H_{01}-mode being bigger than that of the H_{20}-mode. If that criteria is met, the H_{10} mode propagates from f_c to $2*f_c$ uniquely. In Figure 2.6 the field pattern of different modes is shown.

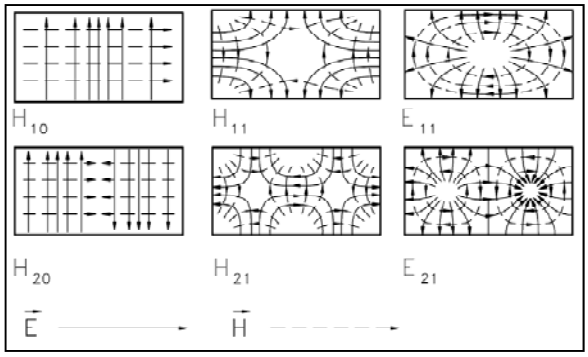

Figure 2.6 Field patterns in a rectangular waveguide [7]

2.3.3 Dispersion

The group and phase velocity in a waveguide is very frequency dependent. Both frequencies depend on the phase constant β_{mn}, which itself depends on the wave number k and the cutoff wave number k_c.

$$\beta_{mn} = \sqrt{k^2 - k_c^2} \tag{2.11}$$

The cutoff wave number depends on the geometry of the waveguide and doesn't change with frequency. The wave number k is given by

$$k = \frac{\omega}{\sqrt{\mu\varepsilon}} = \frac{\omega}{v} \tag{2.12}$$

Where v is the phase velocity of a plane wave in a dielectric with μ and ε, which is the speed of light in vacuum, 299792.458 km/s. If you combine the two formulas above and consider that $\omega_c = v*k_c$ the resulting formulas for the phase and the group velocity are:

$$v_{ph} = \frac{\omega}{\beta_{mn}} = \frac{v}{\sqrt{1 - (\omega_c/\omega)^2}} \tag{2.13}$$

$$v_{gr} = \frac{d\omega}{d\beta_{mn}} = v\sqrt{1 - (\omega_c/\omega)^2} \tag{2.14}$$

At cutoff the phase velocity reaches infinity, whereas the group velocity goes down to zero. With increasing frequency the phase velocity decreases as the group velocity increases. The group velocity always stays below the speed of light, while the phase velocity is above the speed of light. The product of both is the square of the propagation speed in the media.

$$v_{ph} * v_{gr} = v^2 \tag{2.15}$$

In Figure 2.7 the group velocities of the H_{10}(blue), H_{20}(green) and H_{30}(red) modes, normalized to the angular cutoff frequency ω_c and to the speed of light, are plotted. Below the cutoff frequency of a mode the signal can't propagate in this mode, therefore the group velocity is zero. The higher the frequency gets the closer the velocity gets to the speed of light. It can be seen that close to cutoffs of certain modes the group velocity is very low. For the H_{10} it's therefore recommended to work in the range from 1.2*fc up to 1.9*fc, in order to not be close to the cutoff and to ensure that only the H_{10} mode can propagate. This also determines the frequency range used for the reflectometer.

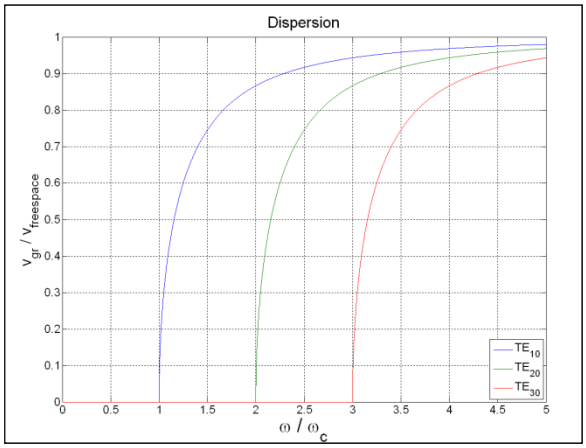

Figure 2.7 Dispersion of TE-modes

It can be seen clearly that signals of different frequencies propagate with different velocities. If a pulse is sent into a waveguide the different spectral components will propagate at different velocities, the pulse will therefore smear after some distance on the line. For the measurements in the frequency domain the need for compensation of the frequency varying electrical length arises, otherwise the phase information obtained will be wrong.

3 Electromagnetic Properties of NEG and Carbon Coatings

3.1 Electrical Properties of Thin Layers

Electrical resistance in a bulk material is mainly caused by three effects. In a perfect lattice due to the wave nature of the movement of electrons they can pass without attenuation. In reality however, no lattice is perfect, electrons always undergo some scattering when moving through a solid. The average distance between two collisions is called the free mean path length.

Even in a perfect lattice without any structural defects or impurities the atoms are not fixed. They vibrate around their mean position, due to temperature. Electrical resistance is also caused by impurity of the material and the resulting defects in the lattice, which cause collisions too. Structural imperfections, such as grain boundaries, cause similar effects as impurities.

The resistivity of a metal film is always higher than that of the corresponding bulk material. Thin film materials generally have a smaller grain size and higher defect concentration than bulk materials [8].

Summing up, there are three main causes for resistivity, movement of atoms due to temperature, and lattice and structural imperfections, which all cause collisions of electrons and create resistance.

So the resistivity consists of two parts, a residual one and a temperature dependent one. There is another effect that has to be taken into account for very thin layers. When one dimension comes close to the free mean path length the scattering of the electrons at the surface starts influencing the resistivity as well. In Figure 3.1 the effect of the layer thickness can be seen. The y axis is the resistivity normalized to the resistivity of the bulk material and the x-axis is the layer thickness relative to the normalized mean free path length, where $k = \frac{d}{\lambda} = \frac{layer\ thickness}{mean\ free\ path\ length}$. Additionally the index p determines the fraction of electrons, which is elastically scattered (they have the same momentum before and after a collision). If p=1 there is no influence from the layer thickness. In reality p lies somewhere between zero and one, the values in Figure 3.1 are derived theoretically, they are very difficult to reproduce in measurements, as it is very difficult

to produce and measure samples of the same material with various precise known layer thicknesses. Nevertheless it shows that the resistance can't be calculated by simply applying Ohms law and can strongly depend on the layer thickness.

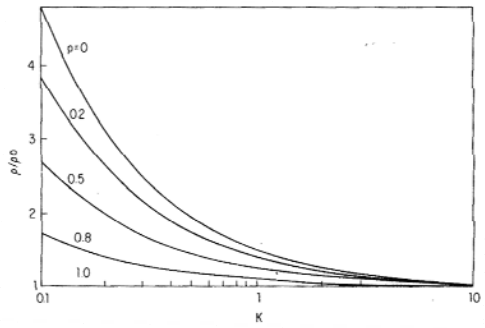

Figure 3.1 Effect of layer thickness [9]

The high frequency properties of a material are influenced by the above mentioned grain structure, the grain size as well as their boundaries. This grain boundary transitions give rise to capacitive effects inside the layer. The coating can then be seen as a series of resistors and capacitors. This capacitive effect can be enhanced by grain boundary oxidation. As different statements on the influence of NEG coating on the impedance are found in literature, the resonator measurements were done to find out if theses coatings are already influenced by the capacitive effects at the frequency range of interest. The same effect could occur at carbon coatings used in the SPS for the same purpose, so they have been tested as well.

3.2 Coatings

3.2.1 General

NEG and Carbon coatings are used to improve the performance of ultra low vacuum systems and to reduce the Secondary Electron Yield (SEY), explained in Chapter 3.2.3. NEG is an alloy of three different elements, 30% Titanium, 30% Zirconium and 40% Vanadium. NEG and Carbon coatings are used in the SPS and Carbon coatings in the warm sections of LHC as well.

3.2.2 NEG Coating Process

NEG is coated via a sputtering technique. This chapter describes the sputtering technique used for the production of the samples on glass rods for the resonator measurements. In Figure 3.2 a simplified drawing of the coating setup is shown. The whole system is inside a vacuum vessel, after the pumping process Argon is inserted, with remaining pressure around 10^{-3} mbar. The samples are placed on a grounded metallic plate above the cathode. The alignment of the samples is also shown in Figure 3.5. The Cathode, consisting of NEG, is placed in the bottom left corner. There is a permanent magnet under the cathode, which creates a magnetic field above the cathode. To the cathode itself a voltage of about -500V is applied. This causes electrons to move towards ground. These electrons then collide with the Argon, resulting in Ar^+ and another electron. Ar^+ is then accelerated by the electric field and moves towards the cathode, where it impacts. The impact of Ar^+ at the cathode causes NEG to be sputtered away from the cathode and deposited on the samples.

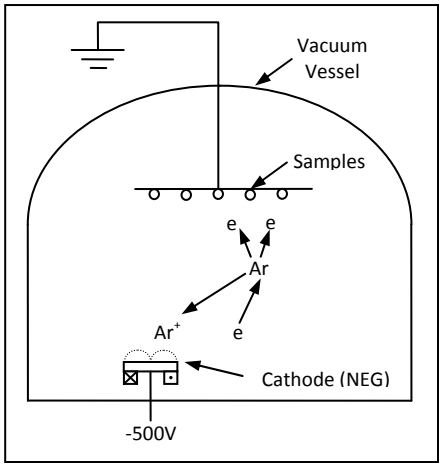

Figure 3.2 Coating setup [22]

The Cathode is above a permanent magnet, this magnetic field traps the electrons above the cathode. This causes most of the collisions with Ar to take place around the cathode and the plasma (the ionized Argon) is exactly where it is needed. The use of the permanent magnet has the advantages of a higher Ionization rate, which enables lower pressure and less collisions of the sputtered NEG with Argon, and that less power is needed as the plasma has just to be setup above the cathode.

In Figure 3.3 the lower part of the vacuum vessel including the two cathodes can be seen. They are below a moveable shutter, which is grounded and used to set up the plasma. Once the plasma is stable they can be removed and the actual coating process starts. Note that only the left cathode was used for the coating process of the glass rods. In Figure 3.4 the cathode without the cover is shown. The cathode itself consists of Zirconium as ground plate, with Titanium and Vanadium inserted as rods. As Titanium shows a lower sputtering rate it covers more surface area than the other two elements, the ratio of the materials surface together with the sputtering rate of the materials determines the composition of NEG.

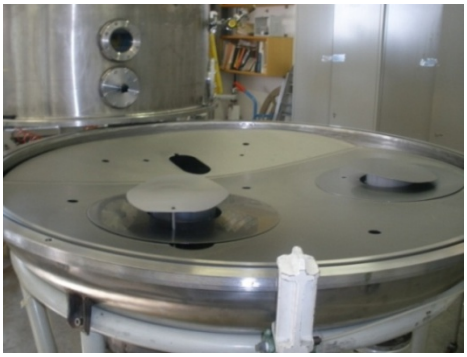

Figure 3.3 Open vacuum vessel[10]

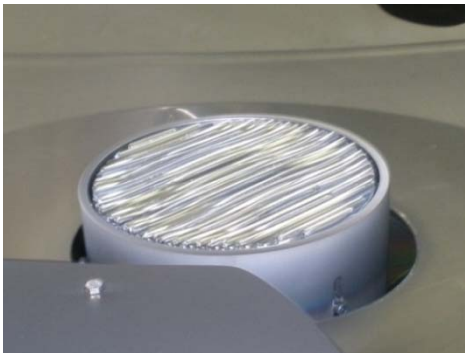

Figure 3.4 Cathode (NEG) [10]

In Figure 3.5 the alignment of the samples is shown. In order to obtain different thicknesses the samples are placed at different distances from the cathode. Beside the samples (glass rods) a glass plate is mounted with a small iron plate on it. After the coating process the iron plate is removed and we obtain a sharp edge, which can be measured with a step profiler in order to obtain the coating thickness of the samples. In Figure 3.6 a picture taken of the plasma during the coating process can be seen.

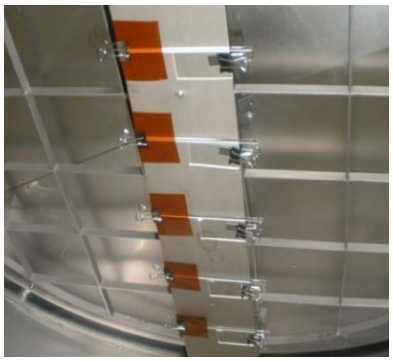

Figure 3.5 Sample alignment[10]

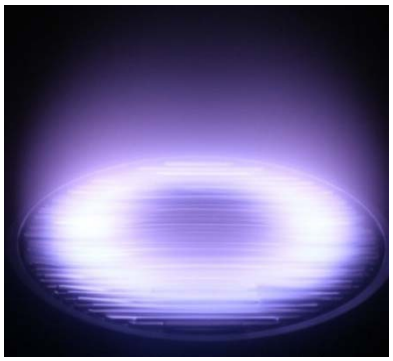

Figure 3.6 Plasma over magnetron[10]

3.2.3 Secondary Electron Yield

If a surface is exposed to electron bombardment surface electrons are released by the impacts and escape. The Secondary Electron Yield (SEY) is a measure of the ratio of the average number of electrons that are released by one impacting electron.

For high intensity particle accelerators this topic has become an important issue, due to a phenomenon called electron cloud effect, which can have a major impact on the performance of the machine. Free electrons will always be present in an accelerator, coming from residual gas, ionized by the beam, synchrotron radiation or lost particles hitting the beam pipe. These electrons are then accelerated by the wakefield of a bunch moving towards the center of the beam pipe. The electrons are then trapped in the center for the length of the bunch, but at the beginning and at the end of a bunch the accelerated electrons eventually hit the beam pipe and release other electrons. They themselves can be accelerated by the next bunch. This can lead to a resonant build up of free electrons, causing the electron clouds.

There are several factors influencing the phenomena one of them being the photoelectron yield. A high photoelectron yield will enhance the release of seed electrons. The photon reflectivity causes the reflection of the synchrotron radiation that can then free electrons elsewhere. To reduce this effect the LHC beam-screen has a saw-tooth-like pattern, where it is hit by most of the synchrotron radiation. The most important parameter for the build-up of electron clouds is the SEY, as a high SEY allows seed electrons to free other electrons. Therefore a lot of research is done to reduce the SEY of materials [11]. As Carbon and NEG coatings show a very low SEY they are of particular interest.

3.3 Cavity perturbation Method

3.3.1 General

A commonly used method for determining the electromagnetic properties of materials at microwave frequencies is the cavity perturbation method. The cavity perturbation method has the advantage of measuring the permittivity as well as the permeability, depending on the place of sample insertion, contactless and non destructive. Another advantage as well as a requirement is that the sample is small in comparison to the volume of the resonator. One of the approaches made for the evaluation of the permittivity is that the sample doesn't change the field in the resonator. Therefore the method can only be applied if the changes in resonant frequency and Q-factor of the resonance peaks are small.

3.3.2 Resonating Cavity

The frequency range of interest was around 3 GHz, so for the measurements an S-Band Resonator was used. The resonator is build from a standard S-Band waveguide and two coaxial to waveguide transitions, modified to provide weak coupling in order to get a resonator and not a short transmission line. In the middle of the resonator, a small hole for sample insertion is placed.

The frequencies of the resonance peaks depend on the dimensions of the resonator, in our case, 72mm width (w) 34mm height (h) and 315.3mm length (l).

The wavelength of a TE_{10p}-mode, where the index p refers the number of standing half waves, depends on the dimensions as follows.

$$l = \frac{p * \lambda_g}{2} \tag{3.1}$$

Where λ_g is the guided wave length, which can be calculated by

$$\lambda_g = \frac{\lambda_0}{\sqrt{1 - \left(\frac{\lambda_0}{\lambda_c}\right)^2}} \tag{3.2}$$

Where λ_0 is the wavelength in free space and λ_c is the cutoff wavelength, which depends on the width of the cavity as $\lambda_c = 2 * w$. Taking into account that $\lambda_0 = \frac{c_0}{f_p}$, with c_0 the speed of light, and solving the equations for f we obtain

$$f_p = \frac{c_0}{2} * \sqrt{\left(\frac{1}{b}\right)^2 + \left(\frac{p}{l}\right)^2} \tag{3.3}$$

For the cavity used with the dimensions given above the results of the calculation of frequencies of the different modes and the measured values are shown in the table below. The measured values are slightly smaller than the calculated ones. This is due to the limited precision of the measurement of the dimensions of the cavity.

Mode	f_{calc} [GHz]	f_{meas} [GHz]
TE_{101}	2.1370	2.1315
TE_{102}	2.2903	2.2878
TE_{103}	2.5253	2.5209
TE_{104}	2.8216	2.8145
TE_{105}	3.1620	3.1566
TE_{106}	3.5338	3.5285
TE_{107}	3.9281	3.9211

The electric field pattern inside the cavity depends on the number of half waves p along the length axis of the resonator and is given by:

$$\begin{gathered} E_x = E_z = 0 \\ E_y = E_0 * \sin\left(\frac{\pi}{b} * x\right) * \sin\left(\frac{p * \pi}{l} * z\right) \end{gathered} \tag{3.4}$$

The z-axis corresponds to the direction of propagation, which is parallel to the length of the cavity, the y-axis is in the direction of the height and the x-axis across the width of the resonator. There is only an electric field along the y-axis, which depends sinusoidal on the other two axes. In Figure 3.7 the pattern of the electrical field of the TE_{103}-mode can be seen.

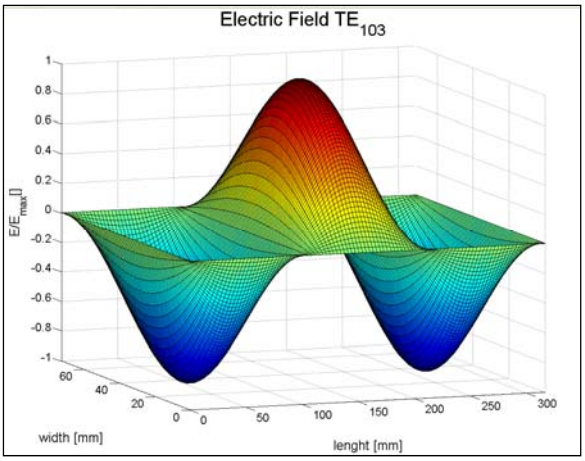

Figure 3.7 Electric field pattern of TE_{103}-mode[10]

3.3.3 Determination of Complex Permittivity of Materials

The basic idea of the cavity perturbation method is to add a small sample with unknown electromagnetic properties. The method is described in countless papers like [12][13][14][15][16] and [17]. The sample will then detune the resonator in a way according to its properties. The approach is to not disturb the electric and magnetic field by the sample, therefore the sample has to be small, but it also has to have a minimum size in order, for its effect not to disappear in measurement uncertainty. The sample is inserted in the regions of the maximum electric or magnetic field respectively, where only one field, either the electric or magnetic, is present. Therefore the electric and magnetic properties of a sample can be measured independently. In both cases a change in the resonant frequency f_r and energy content W, respectively the Q-factor, occurs. For a small detuning the following formula is valid

$$\frac{\Delta f_r}{f_r} = \frac{\Delta W}{W} \tag{3.5}$$

The equation above is the basis for the calculation of perturbations. All quantities Δf_r, f_r, ΔW and W are complex values, the imaginary part of f_r and W can be neglected as the losses in the resonator are very small and the Q-factor is high. The change of energy content ΔW and the energy content W itself can be calculated by the electric and magnetic field strength E and H. The changes in resonant frequency and Q-factor are the measured values.

$$\frac{\Delta f_r}{f_r} = \frac{f_{r_s} - f_{r_e}}{f_{r_e}} = \frac{-\mu_0 \int_{V_s} \left(\underline{\mu}_r - 1\right) \vec{\underline{H}}_e * \vec{\underline{H}}_s^* dV_s - \varepsilon_0 \int_{V_s} \left(\underline{\varepsilon}_r - 1\right) \vec{\underline{E}}_e * \vec{\underline{E}}_s^* dV_s}{2 * \epsilon_0 \int_{V_c} \vec{\underline{E}}_e * \vec{\underline{E}}_e^* dV_c} \tag{3.6}$$

In equation 3.6 the index s refers to the sample and the index e to the empty cavity. Hence f_{rs} is the resonant frequency of the empty cavity and H_e and E_e are the magnetic and electric fields of the empty cavity. The same is valid for the sample with the index s. V_s is the volume of the sample and V_c is the volume of the (empty) cavity. If the sample is inserted vertically into the cavity with the electric field tangential to the sample, the perturbation through the sample is small and it can be assumed, as a good approximation, that the fields in the cavity with and without the sample are equal $E_e = E_s$. To measure the permittivity of the sample, it is placed in the center of the resonator and only the odd peaks are considered, as the maximum of the electric field is in the center. For the calculation of the permittivity the influence of the permeability can be neglected as the magnetic field is zero at the maximum of the electric field. Equation 3.6 can then be simplified to

$$\frac{f_{r_s} - f_{r_e}}{f_{r_e}} + j\frac{1}{2}\left[\frac{1}{Q_s} - \frac{1}{Q_e}\right] = \frac{-\left(\underline{\varepsilon}_r - 1\right) \int_{V_s} E_e^2 \, dV_s}{2 \int_{V_c} E_e^2 \, dV_c} \tag{3.7}$$

Assuming that the electric field in the sample is constant, as an approximation of first order, with negligible errors for small samples, and solving the volume integrals the equation 3.7 can be written as

$$\frac{f_{r_s} - f_{r_e}}{f_{r_e}} + j\frac{1}{2}\left[\frac{1}{Q_s} - \frac{1}{Q_e}\right] = -\left(\underline{\varepsilon}_r - 1\right) * 2 * \frac{V_s}{V_e} \tag{3.8}$$

Comparing the real and the imaginary part we obtain

$$\begin{aligned} \varepsilon_r^{'} &= 1 - \frac{f_{r_s} - f_{r_e}}{f_{r_e}} * \frac{V_e}{2V_s} \\ \varepsilon_r^{''} &= \left[\frac{1}{Q_s} - \frac{1}{Q_e}\right] * \frac{V_e}{4V_s} \end{aligned} \tag{3.9}$$

It has to be considered that the formulas are derived subject to a few approximations and are only valid for small perturbations.

To sum up the above derived formulas, a dielectric material causes a decrease in resonant frequency and the losses cause a smaller Q-factor. If a good conducting material is inserted the resonant frequency will increase and the peaks will be damped. A bad conductor will just cause a decrease of the Q-factor.

3.4 Resonator Measurements

3.4.1 Measurement Setup

For the measurement, the cavity described in chapter 3.3.2 was used. For the analysis a VNA in transmission mode was used. In Figure 3.8 the measurement setup can be seen, the two Ports of the VNA are connected to the two coaxial to waveguide transitions, which are modified to provide only weak coupling. In Figure 3.9 the resonator is shown and in the right part of the picture, the sample holder, situated in the middle of the resonator with a glass rod inserted, can be seen.

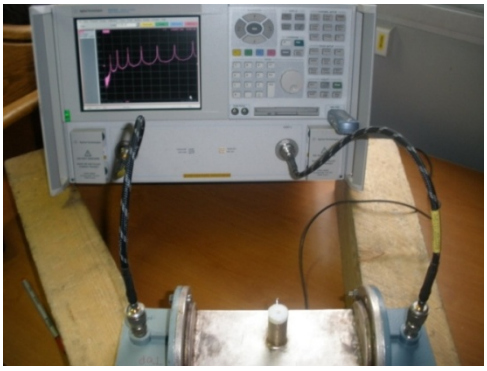

Figure 3.8 Measurement setup [10]

Figure 3.9 Sample inserted[10]

To obtain the resonant frequencies and the Quality- or Q-factor of each peak, S_{12} was measured. At first a scan over the whole frequency range of the TE_{10}-mode of the resonator was performed, to determine, which peak belongs to which mode and to get a basic overview. Then a zoom on the single peaks was made in, so that the maximum was in the center of the screen and that the -3dB points, which are necessary for the calculation of the Q-factor, are captured

with good resolution as well. The data is then stored as a *.s1p – file for further analysis on the PC.

The evaluation of the peaks was made in MATLAB. To achieve greater precision for the resonant frequency the maximum of the curve was not taken, as the maximum itself can be superimposed by noise, which can result wrong frequency readout. Furthermore the -3dB points were determined and a corrected resonant frequency was obtained by calculating the center of gravity between these two points, which reduces the influence of noise.

The Q-factor can be calculated by:

$$Q = \frac{f_0}{B} = \frac{f_0}{f_2 - f_1} \tag{3.10}$$

A short MATLAB function, making it more convenient to evaluate a great amount of data, was applied to obtain the resonant frequency and the Q-factor, both from measurements and simulations.

To measure the permittivity of the coatings, glass rods have been used, as these have very small losses and therefore the change in the Q-factor due to the glass is small. As the glass rods themselves detune the resonator and each glass rod is slightly different in geometry and permittivity, each glass rod was measured before the coating was done.

To check the results of the measurement the permittivity of the glass rods was analyzed too, the results are presented in chapter 3.4.4. The empty resonator was the reference for the detuning of the glass rods. As the coating is done on the glass rods and we are interested in the properties of the coatings the resonator including the glass rods served as a reference for the analysis of the electromagnetic properties of the coatings. The measurement results are presented in the following chapters.

3.4.2 Result of NEG Coating

For the evaluation of the electromagnetic properties of NEG coatings 5 glass rods were coated as described in chapter 3.2.2. Through the different distances to the cathode different thicknesses were obtained, ranging from 0.35µm to 1.6µm.

For further discussion only one rod is considered, as all five rods showed very similar behavior. In Figure 3.10 the results of the measurements of a NEG coated glass rod is plotted.

The black curve is the result of the S_{12} measurement of the empty resonator and the red curve shows the NEG coated glass rod. The peaks are shifted up in frequency, showing the behavior of a conductor, so it can be excluded that NEG has a very high dielectric constant. Beside the frequency shift the peaks are highly damped, to an extent to make the first peak hardly visible, resulting in a precise evaluation of the resonant frequency and the Q-factor of the peak being impossible.

To confirm the measurement results a brass rod with 4mm diameter, same diameter as the glass rods, was measured and simulated. The blue curve shows the results of the simulation and the magenta one the measured data. The reason for comparing the effects of the coating with the effects of a full rod is rather simple. Due to the skin effect the effective conducting layer of the brass rod is also rather thin, for a frequency of 2GHz skin depth of brass is then around 2.97 µm, which is not even the double of the thickest coating with 1.6 µm.

The simulated and measured data of the brass rod agrees quite well. Due to the higher resistivity of NEG the losses are higher and the peaks are much smaller than for brass.

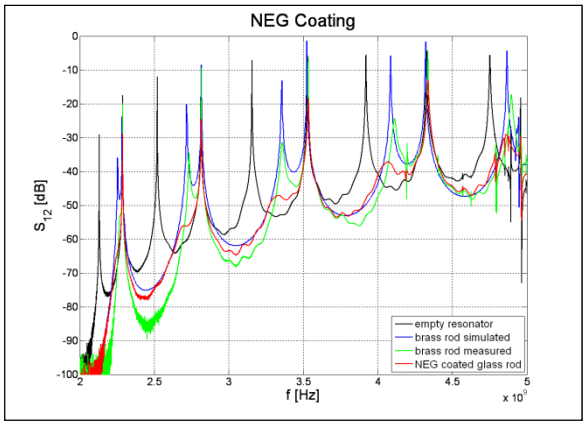

Figure 3.10 Measurement NEG coated glass rod

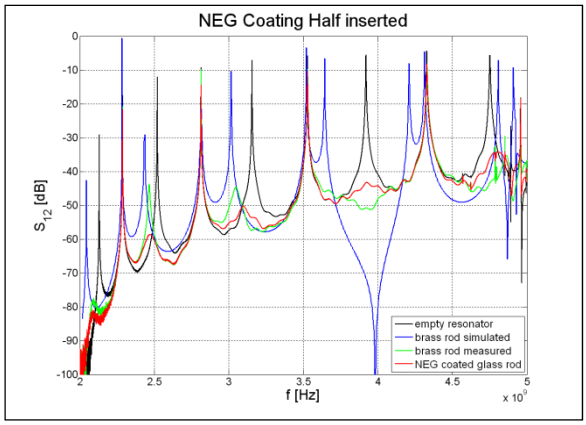

Figure 3.11 Measurement NEG coated glass rod half inserted

To reduce the effects of the losses of NEG on the peaks and to make them more visible a second measurement with the samples only half inserted was performed. The result of the measurements is plotted in Figure 3.11. Again a brass rod was measured and simulated for comparison. This time the peaks are shifted down in frequency due to capacitive effects of the half inserted samples. But this measurement has the advantage of additional visible peaks in the NEG measurement. The behavior of NEG corresponds again to the one of brass and the peaks are also more damped than the ones of brass, but the shift in resonant frequency is again nearly the same, which confirms that NEG behaves purely resistively at these frequencies. The data above 4GHz cannot be considered for evaluation, as the other modes can already propagate, and mode conversion can occur, especially with half inserted samples. To show the entire trend the data is plotted until 5GHz, as for the glass rods no mode conversion seems to occur and the coupler does not excite the TE_{20}-mode. The TE_{109} peak has also been evaluated in the following measurements to gain more information.

3.4.3 Result of Carbon Coating

The same rods as used for the NEG-coating measurements were used for the carbon coatings. Here the same approach was made, the resonator together with the uncoated glass rods are the reference for the carbon coating measurements. Again the glass rods were measured before and after coating and the resonance peaks were analyzed. The carbon coating of the glass rods was a byproduct of another coating process. Therefore only two rods have been coated, having thicknesses of 0.16 µm and 0.21 µm.

In Figure 3.12 the results of the measurement of the carbon coated rods are shown. Again the black curve represents the empty resonator, the blue curve represents the result of the glass rod and the red curve is the carbon coated glass rod. Retailed examination shows that there is a downshift in resonant frequency for the glass rods, which represents the reference for the measurement of the coatings.

The carbon coating causes the odd peaks to be damped. The even peaks do not change, as they do not have any electric field in the region of the sample.

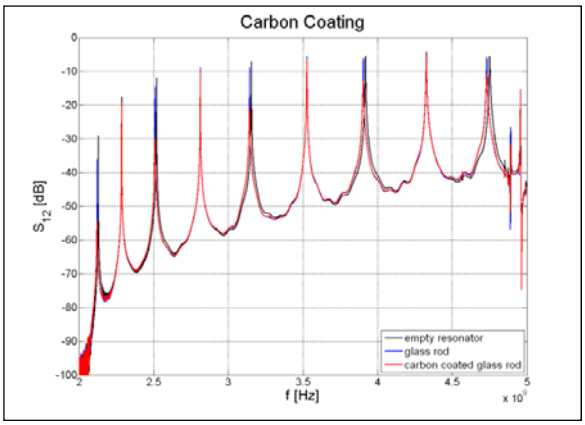

Figure 3.12 Measurement carbon coated glass rod

Carbon coatings also behave resistively, as they damp the peak. It cannot be determined whether a shift in the resonant frequency occurs, as the temperature dependence of the resonator already plays an important role, when looking at such small changes.

The waveguide is made of brass, which has a temperature coefficient of thermal expansion of 18.4E-6/°K, which results in a detuning due to temperatures of -39.3kHz/°K for the TE_{101}-mode

up to -87.6kHz/°K for the TE_{109}-mode. Assuming that carbon has a real dielectric constant of 100 the frequency shift of the TE_{101}-mode would be -18 kHz, which is equal to the change in temperature of half a degree. The change in volume due to the thermal expansion of the glass rod will also have an influence on the detuning and the evaluation of the data.

So it is nearly impossible to measure the real part of the dielectric constant precisely in that region, even if the resonator is temperature stabilized.

If carbon would show a dielectric constant as high as 1000, it would be possible to measure it with acceptable precision, but as just a small detuning, which can be due to temperature and permittivity was measured, it can be assumed that the real part of the dielectric constant is smaller than 1000.

As only dielectric constant as high as 1000 could have serious influence on the impedance of SPS and LHC it can be excluded that the coatings tested will have an influence on the impedance.

To determine the conductivity the change in Q-factor has to be evaluated, as described in chapter 3.3.3. In Figure 3.13 the imaginary part of the complex permittivity is plotted. The curve decreases with frequency, as the complex permittivity is defined as:

$$\underline{\varepsilon} = \varepsilon_0 \underline{\varepsilon_r} = \varepsilon_0(\varepsilon_r' - j\varepsilon_r'') = \varepsilon_0 \varepsilon_r' - j\frac{\sigma}{\omega} \tag{3.11}$$

As we are interested in the conductivity itself, it can be calculated by:

$$\sigma = \varepsilon_0 \varepsilon_r'' \omega \tag{3.12}$$

In Figure 3.14 the result of the measurement of the conductivity can be seen.

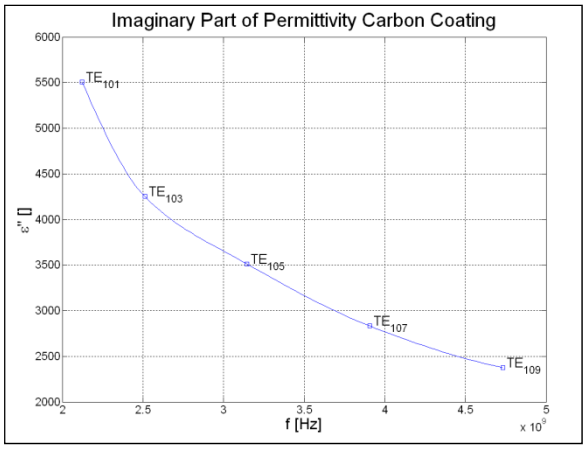

Figure 3.13 Imaginary part of permittivity carbon coating

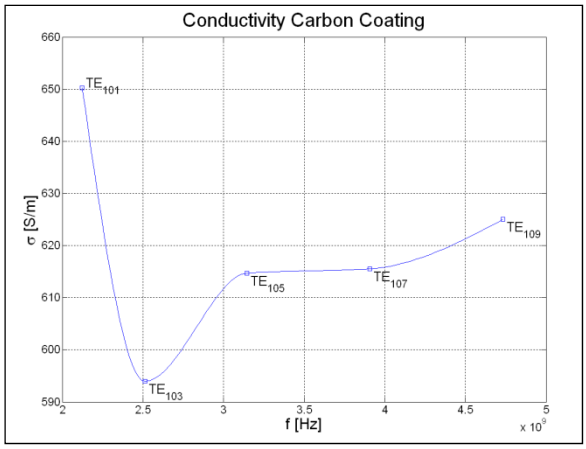

Figure 3.14 Conductivity carbon coating

The values vary around 615 S/m, which corresponds to a sheet resistance of about 7.7kΩ. Average values for the sheet resistance of carbon coatings measured at DC are around 1kΩ[18], the value of 7.7kΩ is still within the variation of resistivity caused by different coating parameters and a relatively thin layer of 0.21 µm.

The relatively large variation of the conductivity over frequency was also observed at the evaluation of the permittivity of the glass rods and will be described below.

3.4.4 Glass Rods

To check the validation of the method and the applied formulas the permittivity of the glass rods themselves was determined. The result of the measurement of the real part of the permittivity is plotted in Figure 3.15. The curve shows a similar pattern to that of the conductivity of the carbon coating. There is a relatively high variation with frequency, respectively different modes. For the simulation an ε_r=4.18 was used, so the most common used TE_{103}-mode shows the smallest error.

In the derivation of the formulas the integral of the electric field in the sample was simplified and it was assumed that the electric field is constant. This makes the formulas valid for every mode and dimensions of the cavity, although in reality the electric field depends on those parameters. To exclude errors due to this approximation the integral was solved for all of the modes and correction terms have been found. The difference is only 0.2% for the TE_{101}-mode

and up to 1% for the TE_{109}-mode. So this approximation cannot be the reason for the relatively high difference between the different modes.

To check if the measured data is plausible, a simulation in CST Microwave studio was done and the result was a similarly shaped curve. The model used for the simulation does not include the flanges, the dielectric sample holder and the coupling was simplified. This causes the differences between the measured and the simulated data, but both are in good agreement.

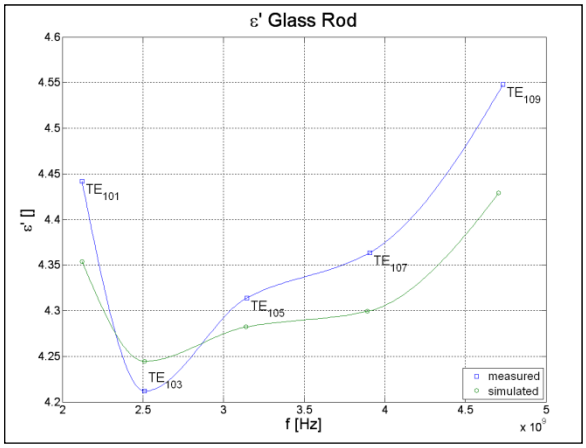

Figure 3.15 Real part of permittivity glass rod

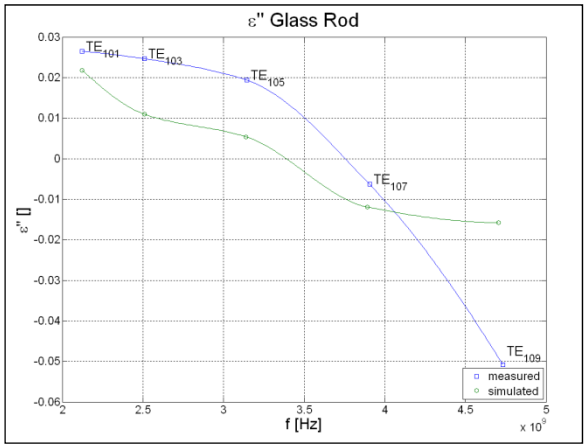

Figure 3.16 Imaginary part of permittivity glass rod

The imaginary part of the permittivity, as plotted in Figure 3.16, reaches even negative values for higher modes. The frequency of the TE_{109}-mode is already above the cutoff of the TE_{20}-mode, but as we excite the oscillation in the middle axis of the waveguide, the TE_{20}-mode is not excided and it gives another measurement point. The data collected at the TE_{109}-mode can't be considered as completely valid. But still gives some hints on how the curve continues.

The simulated data of the imaginary part does not correspond as well as that of the real part to the measured one. This is due to the above mentioned facts and is also enhanced by the use of Perfect Electric Conductor(PEC) as a boundary condition for the cavity walls, which simplifies the calculations. The use of PEC results in the losses in the walls of the cavity not being considered in the calculation. As all these above mentioned simplifications have a impact on the Q-factor the simulated data varies slightly from the measured one.

According to cavity perturbation theory the values should always be above zero, but for the TE_{107}-mode the simulated, as well as the measured value is below zero. These negative values would correspond to negative losses, which is not possible. They are caused by a higher Q-factor with the glass rod inserted. This effect is contrary to expectations and can be explained by image effects on the wall of the cavity, as well as by the fact that more energy is stored in the resonator with the dielectric inserted. Generally the Q-factor is defined as

$$Q = \omega * \frac{Energy\ Stored}{Power\ Loss} \tag{3.13}$$

The influence of the change of the stored energy on the change in Q-factor was neglected in the derivation of the formulas. Image effects of a small sphere have been described in [19] and theses effects are also neglected in the formulas. These image effects cause a change in the wall currents, which in turn changes the losses of the resonator. They also change the field in the resonator slightly and furthermore the stored energy. For a sample with very small losses all these effects start to be an important issue.

A detailed error analysis of the cavity perturbation method was done in [12], but only of the most common used TE_{103}-mode. The above mentioned errors of the different modes, were not treated in this paper, nevertheless it confirms the possibility of an increase of the Q-factor by inserting a dielectric sample into the resonator.

To sum up, even a loss free sample can cause a change in Q-factor. To confirm this, a simulation of a loss free rod with ε_r=4.18, which is the measured value, was performed. In Figure 3.17 the result of the simulation is plotted in red. It can be seen that ε''(imaginary part) is negative for all modes, with large negative values of the TE_{107}- and TE_{109}-mode. These are the two modes, where negative values have been measured.

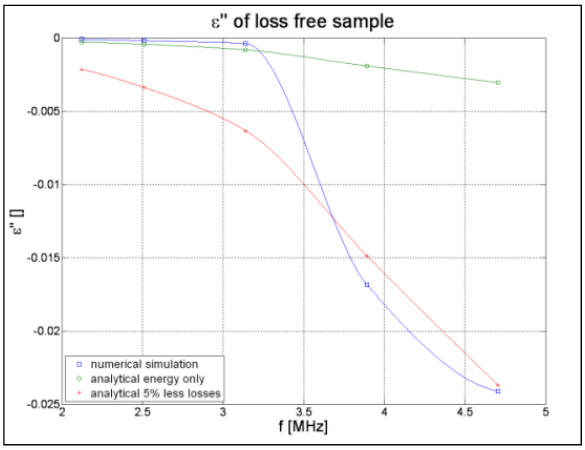

Figure 3.17 Influence of a loss free sample

In addition to the simulation, analytical calculations were done and the results are the green and the blue trace. The green trace just takes the influence of the change in energy stored in the resonator into account and the red one was calculated under the assumption that image effects cause 5% less losses with the glass rod in all modes. The influence of image effects seems to be frequency dependent with approximately a square dependency. Both, numerical simulation and analytical calculation confirm the possibility of a rise in Q-factor due to a loss free dielectric. It can be assumed that a very low loss dielectric such as glass causes the same effects.

The cavity perturbation theory is based on calculations of perturbation, with results of small errors only for small perturbations. Therefore it can be assumed that the 4mm diameter glass rod does not represent a “small perturbation” anymore.

3.4.5 Simulation of the Measured Data

A precise simulation of the cavity perturbation method is rather difficult, as we are interested in very small changes and the sample inserted is very small as well. The mesh used for the calculations had to be a tradeoff between accuracy and calculation time, as for each different parameter, such as sample size, ε_r or tan δ, at least 10 calculations are required. This is due to the accuracy requirements of the resonant frequency and bandwidth. As the band to look at is roughly known, a calculation of the area where the peak is suspected has to be done. Then the calculation has to be repeated with the frequency range set close to the two -3dB points, to have enough points between them to calculate the Q-factor precisely.

It was found that the mesh itself has a non negligible influence on the result, as the inserted sample causes a small detuning and a change of the mesh grid causes similar effects. To avoid this problem for each calculation the empty resonator was calculated with the same mesh grid. First, round samples have been simulated and it was found that the round shape of the samples causes problems and errors due to the difficulty of meshing them. For the second simulation a rectangular sample with the same volume as the round sample was used and the results have been in better agreement with the measured data.

In Figure 3.18 the comparison between the calculation results of the sample with a round and a square cross section is plotted. The two curves are quite similar, but the pattern of the square shaped sample is in better agreement with the measured data. For the calculation of the Q-factor the results differ significantly at higher frequencies as can be seen in Figure 3.19. The result for the square shaped sample reaches negative values, while with the rod the curve increases again, which is definitely due to numerical errors in the calculation caused by the mesh.

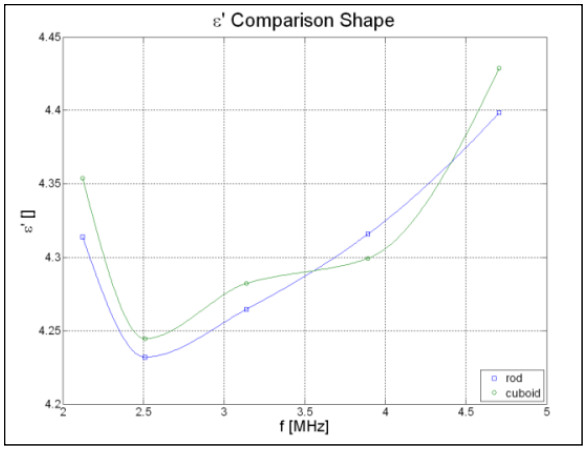

Figure 3.18 Shape influence on calculation of ε'

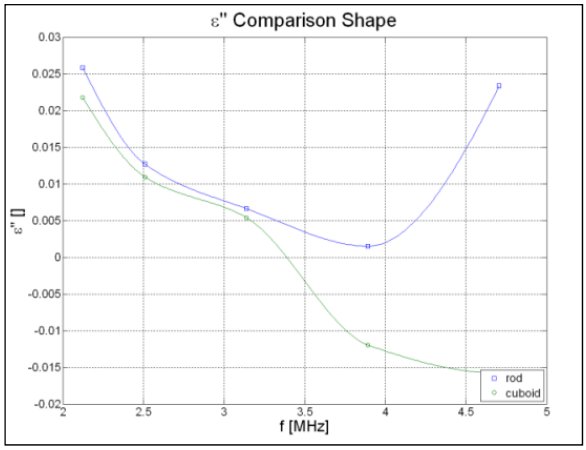

Figure 3.19 Shape influence on calculation of ε''

To be able to measure the properties of the coatings a minimum surface area is required, as the thickness of the coating is limited. The coatings were done on a 4mm glass rod and as we have been interested in ε_r, different values of ε_r have been simulated to evaluate the error.

The result is plotted in Figure 3.20, it can be seen that the TE_{103}-mode shows the smallest error of all modes. Above an ε_r of approximately 4 the error starts to increase rapidly, reaching

unacceptable values. The TE_{109}-mode shows the highest error, but as described above, it is used just for additional information about the continuance of the curve.

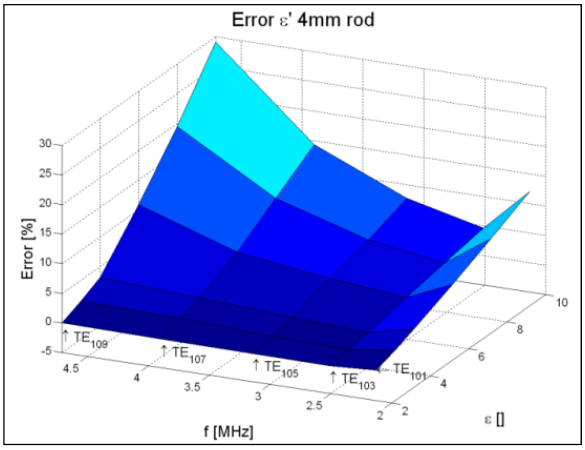

Figure 3.20 Error analysis varying ε

3.4.6 Comparison of NEG and Carbon Measurements

NEG and carbon coatings seem to behave completely differently in the resonator. Carbon coatings just damp the peak slightly and NEG coatings cause a huge detuning. This is due to a different conductivity. NEG coatings are conducting relatively well, with a sheet resistance of the samples below 1Ω, much smaller than Z_0 the impedance of free space with 377 Ω. Hence the NEG coating acts like a short and causes reflections, this is why such a huge detuning of the resonator occurs. Carbon coatings show a much higher resistivity and the samples have sheet resistances of around 7.7k Ω, which are higher than Z_0. Thus they just damp the odd peaks and as they do not cause a measureable change in resonant frequency it can be excluded that they have a huge dielectric constant.

4 Beam-screen Reflectometer Calibration Measurements

4.1 Theory

4.1.1 TDR Time Domain Reflectometry

In electrical transmission lines a signal is reflected at any change of impedance, with reflection according to its size. The two extremes are open and short, where the whole energy of the signal is reflected and returns to the sender. If the transmission line isn't matched properly or there are some faults or discontinuities the pulse will only be partially reflected. An obstacle in the beam-screen acts like a discontinuity for the propagating wave and causes therefore a reflection and through that reflection the object may be detected.

In Figure 1.1 the reflections of the beginning and the end of the line as well as the reflections due to a fault in the middle are shown. The graph already shows the distance to the fault. The delay in time is twice the time the signal needs to travel from the sender to the fault, as it has to travel back to the receiver again.

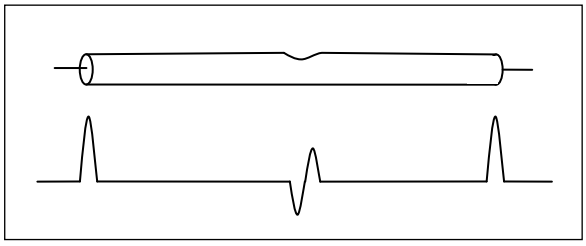

Figure 4.1 Reflections on a line

Time Domain Reflectometry is based on injecting a pulse into a transmission line and recording the response, due to reflections, over time. With the knowledge of the propagation speed the distance from the cause of the reflection can be determined. Modern instruments can achieve precise spatial resolutions below 1mm. This is only valid for a single pulse, 2 close pulses cannot be resolved at such a resolution.

The handling of the signal is here rather simple in comparison to waveguide mode TDR, described in chapter 4.1.2, if applied for a non dispersive media. As a waveguide is used for the

beam-screen Reflectometry, which is a very dispersive media, a pulse will smear out beyond recognition after only a short distance, due to different spectral components propagating at different speeds. Therefore it is difficult to apply TDR using real pulses, which requires complex signal treatment to correct the phase of the different spectral components.

4.1.2 Waveguide mode Time Domain Reflectometry

Instead of injecting a real pulse a synthetic pulse is used. In other words this means the responses of the spectral components of a real pulse are recorded over a certain frequency range. The data is then transferred back into the time domain using the inverse Fast Fourier Transform (iFFT). Instead of a fast DC step, a short RF-Burst, shown in Figure 4.2, containing spectral components over the frequency range measured, is the equivalent time domain signal. As the RF-Burst is very short, it is more convenient to look at the hull curve in time domain, this makes the display and furthermore the method equivalent to real time TDR using a short pulse of the same length.

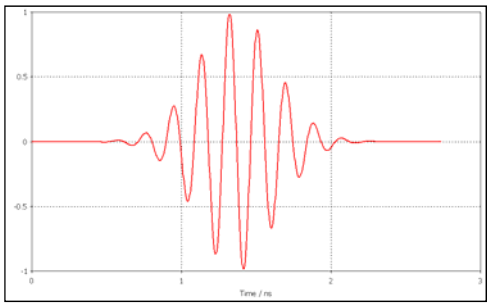

Figure 4.2 RF-Burst

In general both methods, waveguide mode TDR and real time TDR, are equal, but working in the frequency domain offers some advantages. One of them is the sampling of the raw data in the frequency domain, which enables narrowband filtering and therefore a better Signal to Noise Ratio (SNR). As the obstacles can be considered as stationary, the measurement time is not of utmost importance, compared to other applications as for example radar.

Another thing that is done by the beam-screen Reflectometer is the numerical removal of dispersion and frequency dependent attenuation. One important advantage is the precise control of the frequency range worked at and the possibility to easily vary parameters such as

number of points and frequency span, which further more influence the length of the time trace and the spatial resolution. For the measurement, a common network analyzer can be used, and there is no need for additional special equipment. The data processing can be carried out on a modern network analyzer itself, as they run on operating system platforms, or on a PC or Laptop connected to the network analyzer, as done for the Beam-screen Reflectometer.

4.1.3 Beam-screen as a Waveguide

The beam-screen is situated inside the beam pipe, which is shown in Figure 1.2. The function of the beam-screen is to shield the cold bore (1.9K) from synchrotron radiation and to guide the beam induced image currents. To keep the beam-screen at a maximum temperature of 20K two cooling tubes are mounted, one on top and one at the bottom of the beam-screen, as can be seen in Figure 4.3, as well as in Figure 4.4.

The beam-screen is manufactured out of a special stainless steel with a 75µm thick layer of copper coating, to provide a low impedance for the beam induced image currents. To reduce the residual pressure the beam-screen is equipped with 8 rows of pumping slots in a pseudo random pattern, which repeats every 50cm.

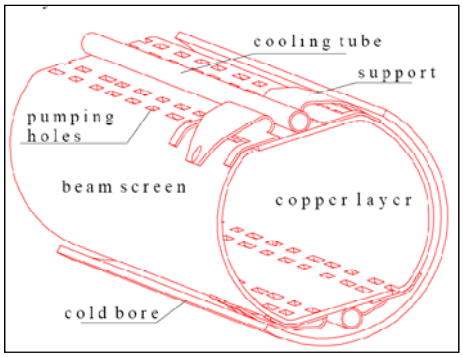

Figure 4.3 Drawing of beam-screen [20]

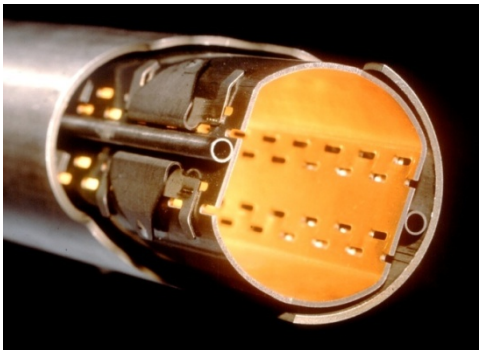

Figure 4.4 Picture of the beam-screen[3]

As the beam-screen's inner surface is coated with copper it is suitable for the use as a waveguide. Due to the non standard geometry of the beam-screen, the different modes and cutoff frequencies can just be approximated analytically. Numerical simulations and

[3]Source: http://oraweb.cern.ch/pls/ttdatabase/docs/F31719/9705015_04.jpg, 15.3.2009

measurements have been performed during the development of the reflectometer [21][22]. Two modes have been chosen for the reflectometer, one is the TE_{c11}-mode (the index c refers to cosine or vertical orientation) and the other is the TM_{01}-mode. These modes will be simply referred to as TE-mode and TM-mode.

These two modes show small interaction with the pumping slots and hence only cause relatively small reflections. Beside the pumping slots mounting supports are situated every 75cm to keep the beam-screen in place in the cold bore. These supports also cause some reflections. The reflections of the pumping slots and the mounting supports represent the “noise floor” or clutter of the reflected signal.

In Figure 4.5 the field pattern of the electric field of the TE mode used is shown, which is similar to the pattern of the TE_{10}-mode in a rectangular waveguide. In Figure 4.6 the field pattern of the magnetic field of the TM-mode is shown, this pattern is quite similar to the field pattern of a coaxial cable.

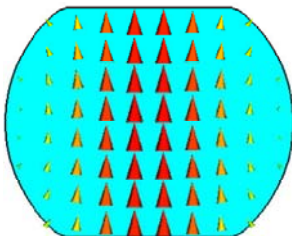

Figure 4.5 TE-mode electric field pattern [22]

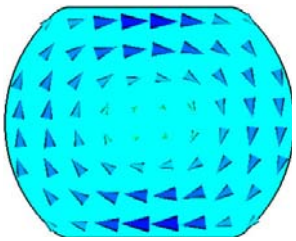

Figure 4.6 TM-mode magnetic field pattern [22]

The two similarities described above have been used to build the coupling structures between the coaxial cable and the beam-screen for the two different modes.

4.1.4 Coupling Structures

In Figure 4.7 a drawing and Figure 4.8 a picture of the TM-mode coupler is shown. As the field pattern of the TM-mode is very similar to the one of a coaxial line the coupler consists of a conical extension of the coaxial line with the inner conductor ending after the enlargement. This can be clearly seen in Figure 4.7. The enlargement of the coaxial line is followed by a smooth transition of the round to beam-screen cross section. In Figure 4.8 the two parts of the coupler,

connected by screws in the middle with the mounting clamp for fast and easy handling on the right can be seen. The TM-mode coupler is used in a frequency range of 6 to 10 GHz.

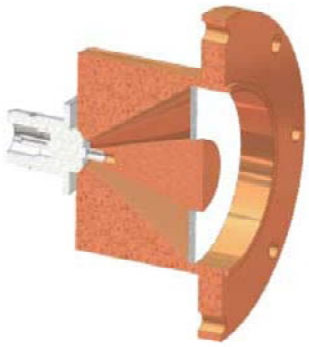

Figure 4.7 Drawing of TM-mode coupler [23]

Figure 4.8 Picture of TM-mode coupler[10]

For the TE-mode another coupler is used. As the field pattern of the TE-mode is very similar to the pattern of the TE_{10}-mode in a rectangular waveguide a standard commercial coaxial to waveguide transition is used. Again there is the need for a smooth transition from the rectangular cross section to the beam-screen, which is shown in Figure 4.9 The whole coupler can be seen in Figure 4.10.

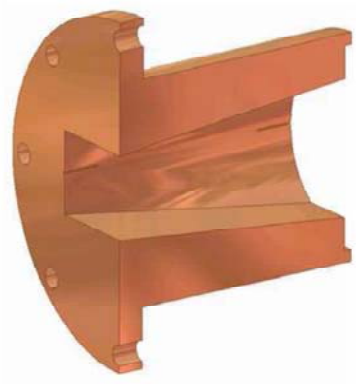

Figure 4.9 Drawing of TE-mode coupler transition [23].

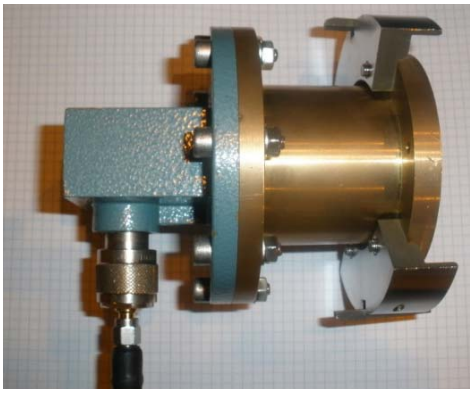

Figure 4.10 Picture of TE-mode coupler[10]

4.2 Measurements

4.2.1 Test Setup

For these measurements a single beam-screen was used, as for the tests obstacles had to be placed inside and removed again. Hence there was a non negligible probability of an object

remaining or of damage to the beam-screen due to the tests, and therefore the use of a complete dipole magnet was out of question. As the beam-screen itself works as a waveguide and there is only very small, negligible interaction with the surrounding cold bore, it was enough to do the test in this setup. Missing are only the mounting supports every 75cm, which cause additional reflections and have influence on the “noise level” or clutter of the reflected signal.

The tests were done in SMI2, the hall where the final assembly of the LHC magnets took place and are then sent to the tunnel. In Figure 4.11 a picture of the setup can be seen. In the middle of the picture, there is the 16m long beam-screen held by wood supports every 5m. At the end of the beam-screen the TM-mode coupler is connected, the other end is left open. The network analyzer is situated in front of the setup and on the left side of the coupler the laptop, on which the analysis software is running, is placed.

Figure 4.11 Measurement setup[10]

The first test done was to determine how sensitive the measurement is to misalignment, or non perfect straightness of the beam-screen. It was seen that the data recorded from several different alignments of the beam-screen, differed just in the order of the changes in general repeatability. The difference between these measurements was in the range of approximately -100dB for both modes, which is 30 to 40dB below the “noise floor” depending on the mode. Therefore a difference in the alignment cannot be detected by the beam-screen reflectometer and it can be excluded that the alignment has an influence on the tests.

To place the obstacles is not a task as obvious as it may seem, the obstacle has to be placed along the beam-screen with a certain accuracy and repeatability. The positioning also should not have taken too long as many samples with different orientations and placements had to be tested. The solution adopted was rather simple and easy to apply in practice. The samples were glued to a small slider and dragged through the beam-screen by a small nylon string, which was constantly kept under tension. To find out, whether the nylon string would perturb the results, a measurement with and without the string was performed. The difference is again comparable to the one of misalignment. The nylon string does not cause any reflections as it does not represent a discontinuity of the beam-screen.

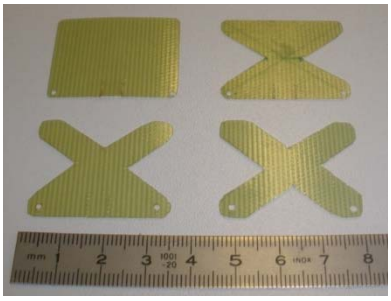

Figure 4.12 Different sliders[10]

As sliders, four different versions have been tested, all of them can be seen in Figure 4.12.

The sliders are made out of a thin sheet of glass fiber and designed to have small reflections. They had to be slightly longer than broad in order to not rotate and get stuck. The “full slider” in the top left corner has the biggest reflections of all. The slider in the top right corner showed much smaller reflections on both modes and is nearly invisible in the TM. This is due to the smoother transition through the conical change in the cross section.

The other two sliders at the bottom showed slightly smaller reflections, but also less mechanical stability, so the slider in the top right corner was chosen as a tradeoff between reflection and stability. Longer sliders, which provide an even smoother transition, were tested as well but the reflections were just slightly smaller. Nevertheless the reflections of all sliders have been so small, that they could only be detected with the help of the reference data from the empty beam-screen. Otherwise the sliders could not have been distinguished from the noise floor. All

following tests have been done with the slider in the top right corner of Figure 4.12 as they cause only small reflections in relation to the obstacles tested and therefore there was no demand for numerical removal.

4.2.2 Basic Reflection of a Dipole Magnet

All magnets show a similar pattern of reflections, but nevertheless they are unique for each magnet, rather like a signature. Once a “signature” of a magnet is recorded it can be used for further comparisons, for example after the cool down, to check if anything has changed. In Figure 4.13 the basic reflections of a single dipole magnet of the TE-mode can be seen. At the beginning there is the initial reflection from the coupler, at the end of the magnet, after about 16m, the entire signal is reflected. Between those two maximum reflections lies the area of interest. In the TE-mode the 50cm and 75cm pattern of the “noise floor”, described in chapter 4.1.3, can be seen clearly. The general noise floor is slightly below -55dB. Every peak above that “noise floor” is suspicious. At about 4.2m and 6.5m two peaks are slightly higher than the others. In this case this is due to the mounting supports, the 75cm pattern. But in some other cases peaks like that could indicate an obstacle. Here we see how difficult it is to distinguish between the “noise floor” and a real obstacle.

In Figure 4.14 the reflections of the TM-mode are plotted. The “noise floor” is about 5dB lower than the TE-mode, this is due to the TM-mode having no radial currents and therefore being less sensitive to the pumping slots. Nevertheless there is another unwanted effect in the TM-mode, the reflection of the end of the line can be seen just short before 16m, but around 14.5m there is another relatively broad peak. This peak is due to mode conversion, as the TM-mode is working above the cutoff of other modes these modes can be excited by the non perfect reflection at the end of the beam-screen. These other modes with lower cutoff frequencies propagate faster than the TM-mode and therefore cause a peak before the original peak, as they arrive earlier.

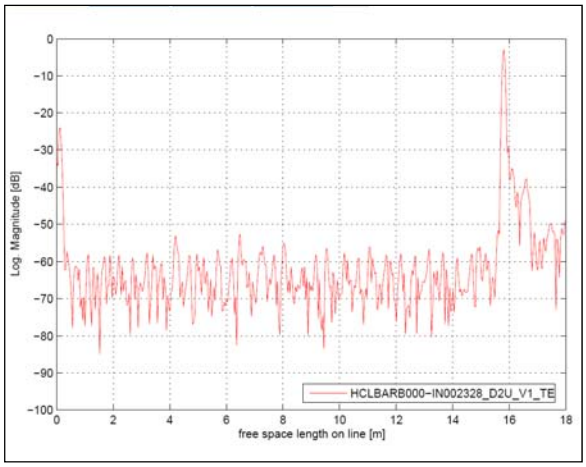

Figure 4.13 Dipole magnet TE-mode

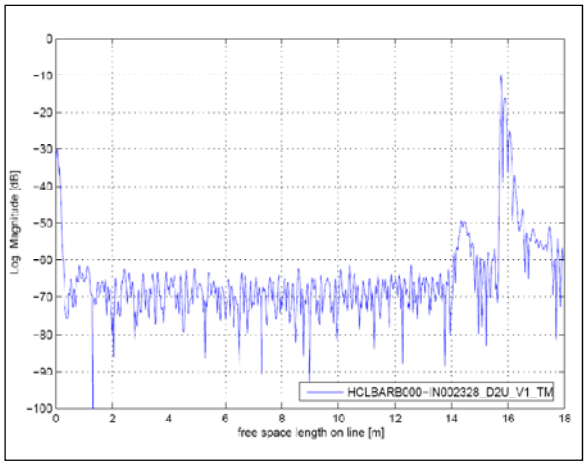

Figure 4.14 Dipole magnet TM-mode

It is difficult to determine whether a peak is due to an obstacle or due to mode conversion. A useful tool to determine peaks caused by mode conversion is the waterfall plot, as can be seen in Figure 4.15. The x-axis represents the length of the line and the y-axis the focused distance, the blue line, which goes across the display, shows the focused data that is plotted in the figures above. The waterfall plot is build by redundant data which comes from the dispersion correction. When focusing for each distance, the iFFT is done over the whole length but only the data of the focused part is used, the rest is stored in a matrix. This matrix can then be plotted as the waterfall plot. As a signal that propagates in a different mode, also propagates with a different velocity, the focusing fails and the peak is smeared out. This can easily be detected with the help of this waterfall plot. Each reflection is shaped like a cone with the center on the focused line. At 14.5m the yellow cone is not in the center of the focused line, hence it can be said that the peak is due to mode conversion.

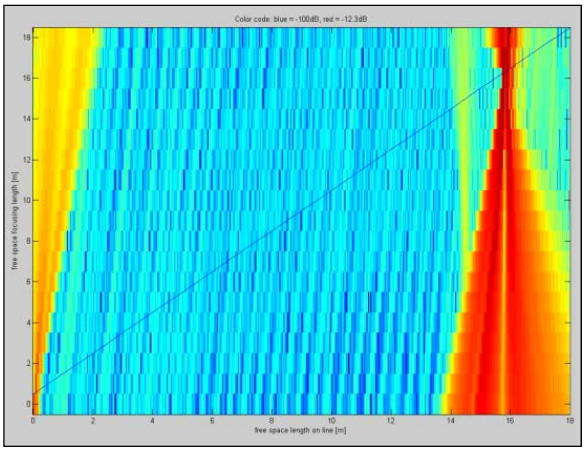

Figure 4.15 Waterfall plot of TM-mode

Mode conversion only occurs in the TM-mode as the TE-mode used is the first and only mode that can propagate at those frequencies. Unfortunately there is a third major problem, namely multiple reflections, which concerns both modes. Multiple reflections are especially a problem when looking at a longer length including more magnets. At each magnet interconnection reflections occur, as the wave travelling back is also reflected by the interconnection and then reflected again by the next one. So a peak can occur where none should be.

4.2.3 Measurement Results

Initially steel spheres of different sizes have been tested to get a first impression of the nature of the reflections. A sphere was chosen because there is no possibility of varying its orientation. Hence the reflection will always be the same at the same location. In Figure 4.16 a picture of a steel sphere with 4mm diameter mounted on the slider and placed at 8m distance can be seen. In Figure 4.17 the results of the TE-mode measurements and in Figure 4.18 the results of the TM-mode measurements are plotted. The sphere can be detected easily with both modes. In TM-mode small peaks before and after the sphere occur due to mode conversion.

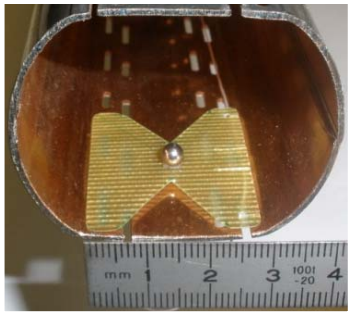

Figure 4.16 Steel sphere Ø4mm

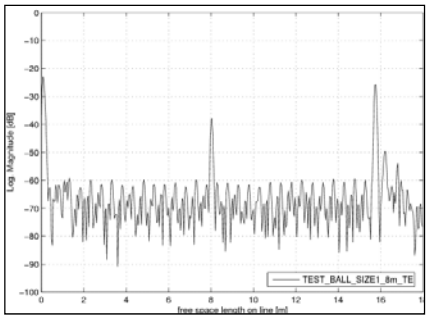

Figure 4.17 Steel sphere Ø4mm TE-mode

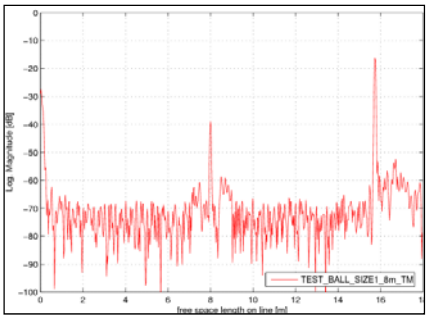

Figure 4.18 Steel sphere Ø4mm TM-mode

The samples have been measured at different distances and a small dependency on the distance, with respect to the "noise floor" pattern, was found. This slightly influences the detection of small obstacles but can be completely neglected for bigger ones, as the variation in reflection size can also be due to misalignment of the samples.

An interesting example for a "small" obstacle is a 10mm long steel wire with a diameter of 1mm placed in the corner, which can be seen in Figure 4.19. The corresponding measurement data is plotted in Figure 4.20 for the TE-mode and in Figure 4.21 for the TM-mode. The sample is placed at 8.4m. In the TE-mode a small peak is visible. It has to be considered that for the tests no mounting supports were used and if the data below is compared to Figure 4.13 it can be clearly seen that the mounting supports can cause similar reflections. For the TM-mode the obstacle is even invisible.

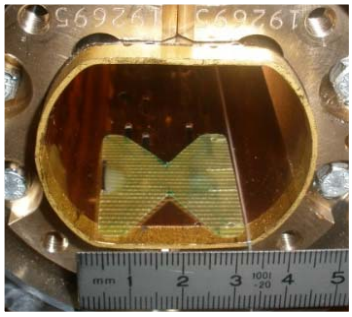

Figure 4.19 10mm steel wire Ø 1mm

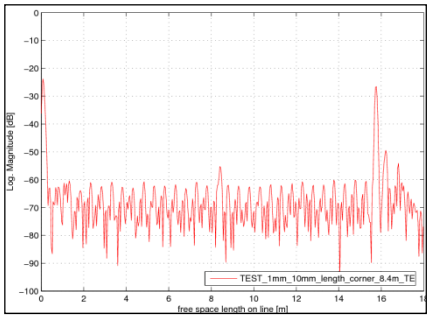

Figure 4.20 10mm wire TE-mode

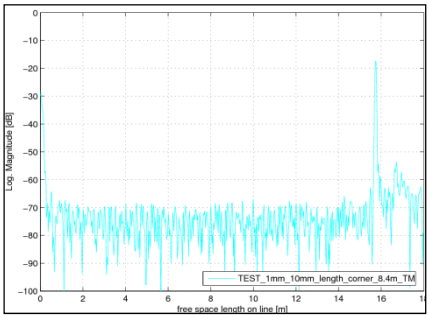

Figure 4.21 10mm wire TM-mode

It will be very unlikely to find such an obstacle in the LHC and if it is present it will not be found by means of beam-screen reflectometry, only a visual inspection with the endoscopy will find it. But this example shows the limits of the system very well although this obstacle could have

serious influence on the LHC. When the magnetic field in the dipole magnets is present the sample will stand up, be hit by the beam and furthermore cause the magnet to quench. Fortunately the sample was recovered from the beam-screen after the measurements and will not be of danger for the LHC.

As beam-screen reflectometry can also be done in-situ, with the vacuum present, it is also performed as a final check, once the magnetic field is applied. Then the rod will stand up as described above to, become comparable to the sample shown in Figure 4.22. There will be a small difference, when placed in the corner, but nevertheless in this orientation it causes completely different reflections than when lying flat in the corner. The rod now behaves like a short for the electric field and it can now easily be detected in TE-mode, plotted in Figure 4.23, and TM-mode, plotted in Figure 4.30.

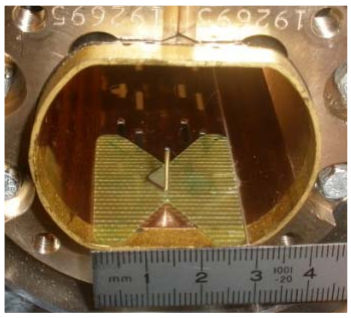

Figure 4.22 wire Ø1mm standing

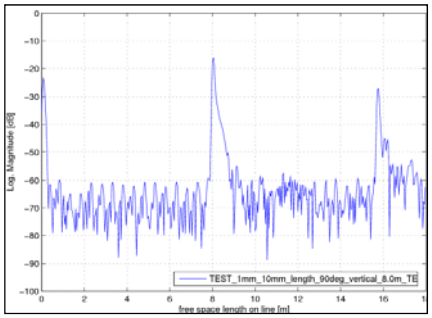

Figure 4.23 10mm wire standing TE-mode

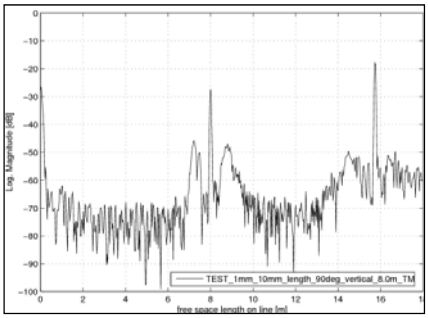

Figure 4.24 10mm wire standing TM-mode

This is probably the most extreme example of orientation and location dependency, but it clearly shows that there is a big dependency on these parameters. This is mainly caused by the shape of the electric field and the huge difference in frontal area, which results in a rather small change in the cross section of the beam-screen.

4.2.4 Mode conversion

The data taken in the test setup in TM-mode did not show mode conversion at the end of the line, when no sample or only a small sample, as can be seen in Figure 4.14 and Figure 4.21, was present. For a huge sample like in Figure 4.24 a peak due to mode conversion at the end of the line is visible, but the actual mode conversion takes place at the sample and not at the end of

the line. This observation gave rise to the question why in all the TM-mode measurements, data taken from dipole magnets, even without obstacles, showed mode conversion.

The answer is rather simple, the extremities of the beam pipes are usually covered with protection caps, as can be seen in Figure 4.25. All the measurements for the final inspections on the surface were performed with theses protection caps. A signal is reflected by a perfect short and an open end in the same way, beside the phase. As for the measurement only the amplitude is considered and they should give the same result. It was assumed that the aluminum protective cap, as it is well conducting acts like a short, but in reality there is a gap of 4 to 5mm between the end of the beam-screen and the cap. In fact the cap terminates the line more like a resonant cavity, which enhances mode conversion, than as a good short.

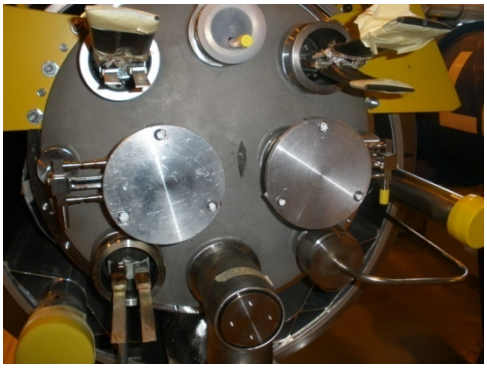

Figure 4.25 Magnet with protection caps[10]

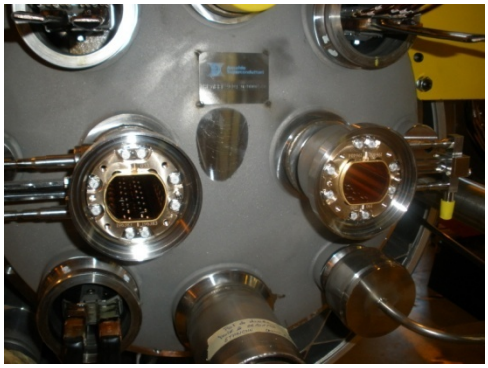

Figure 4.26 Magnet without protection caps [10]

To test the influence of the protection cap, measurements without the cap, as can be seen in Figure 4.26, were performed. The results for the TE-mode are plotted in Figure 4.27 and for the TM-mode in Figure 4.28. The influence on the TE-mode is very small, only the final reflection from the end of the line is smaller without the cap (green). For the TM-mode the result is totally different, the peaks that occur at that end of the line through mode conversion (blue), disappear completely once the protection cap is removed (green).

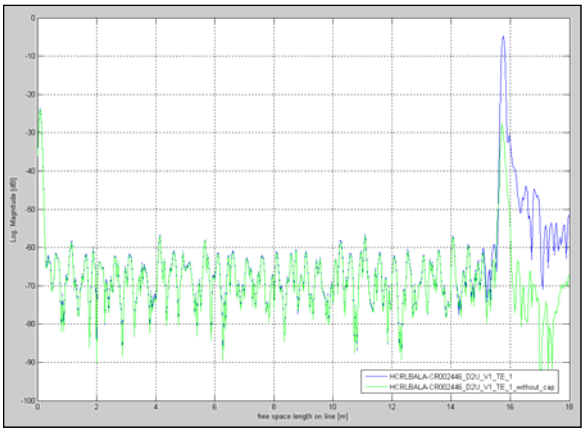

Figure 4.27 Influence of protection cap TE-mode

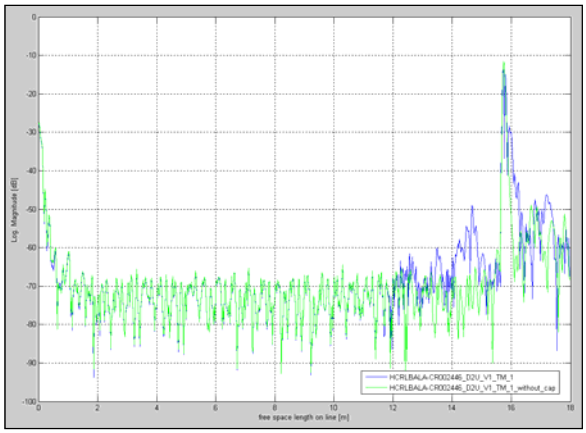

Figure 4.28 Influence of protection cap TM-mode

Future measurements will be performed without the protection cap, in order to avoid the "blind spots" caused by mode conversion. But this only affects the final inspections on the surface, once the magnets are connected in the tunnel, the interconnection between them cause the same effects, which cannot be avoided.

4.2.5 Correlations

To get information useful to estimate which reflection could be due to which object, the recorded reflections of objects depending on their size where plotted. In Figure 4.29 such a correlation of the sphere sizes with the corresponding reflections of the TE-mode is shown, the same is plotted in Figure 4.30 for the TM-mode.

Once a reflection is measured, it can be quickly determined by looking at the horizontal axis to which object the measured data could belong. Nevertheless it can just be used as a reference to determine which objects of which size and location causes which reflections. To determine between different objects, showing the same value of reflection is impossible.

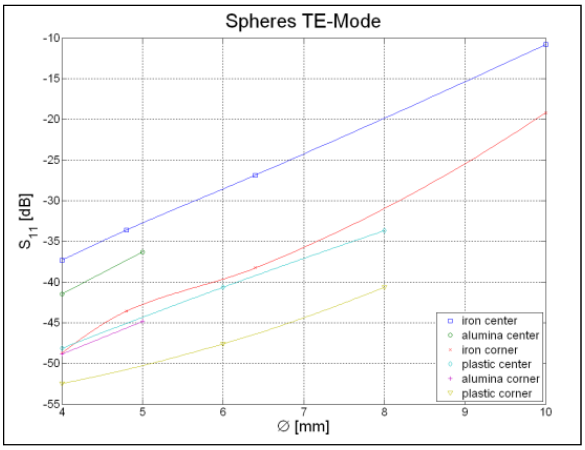

Figure 4.29 Spheres TE-mode

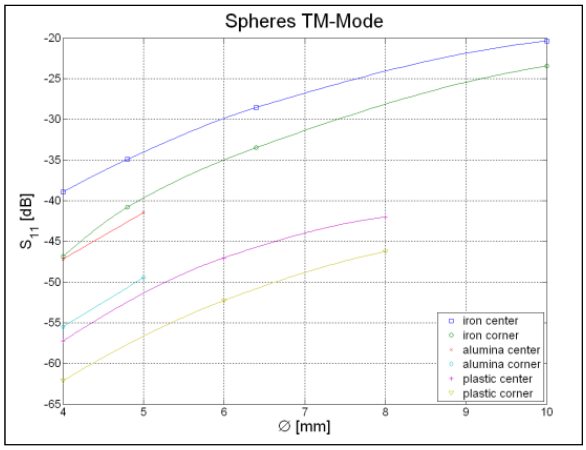

Figure 4.30 Spheres TM-mode

The TE-mode is more sensitive to changes of the diameter of the spheres, the reflection increases with approximately a cubic dependency, whereas the TM-mode starts to show "saturation" for higher diameters. This is mainly due to the different field patterns of the TM-mode and to the fact that regions with smaller fields are reached when increasing the diameter.

In Figure 4.31 it is easier to compare the two modes, as the samples have been placed in the center, where both modes have their maximum electric field.

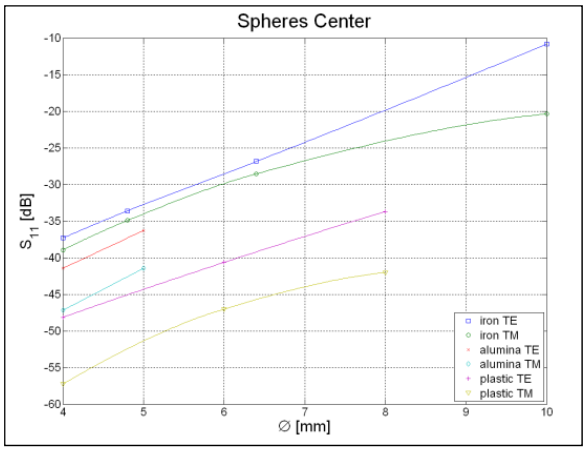

Figure 4.31 Spheres center

For the steel spheres both modes are nearly equally sensitive, beside the effect of "saturation" for higher diameters. The effect of "saturation" does not matter at all, as the measurements are to detect obstacles and not to determine their size and this reflections are clearly above the level where a peak will be considered as a peak. For the alumina spheres the signal from the TE-

mode is around 5dB above the one from the TM-mode. The steel spheres interact with the magnetic and electric field, therefore both modes are nearly equally sensitive. Whereas the alumina spheres just interact with the electric field, therefore the TM-mode is less sensitive.

The same is true for the plastic spheres, beside the fact that they show smaller reflections due to a smaller dielectric constant.

5 Conclusion

5.1 NEG and Carbon Coatings

Both coatings show purely resistive behavior. Therefore the coatings behave then like a bad conductor on a good one, causing the current to flow mainly on the surface of the good conductor as the bad one has a very high skin depth and high resistivity. Hence only a small part of the current will go through the coating and furthermore the increase in impedance will be very limited even negligible. Therefore it can be assumed that the coatings tested do not have any influence on the transversal beam coupling impedance of SPS and LHC. The different statements about NEG coatings can be explained by the fact that facilities, where an influence of NEG on the impedance occurred, are working with very short bunches with spectral components of up to 100GHz. It can be the case that NEG as well as carbon coatings may show dielectric behavior at such frequencies.

As the coatings were made on glass rods with a rather smooth surface the grain size of the coatings tested is rather small. It cannot be excluded that the coatings made in magnets have a larger grain size. This strongly depends on the surface of the base material, as well as on various coating parameters [24]. As these capacitive effects can also depend on the grain size, this could also be the reason for the different statements in literature and it cannot be excluded that coatings with larger grain size as the ones measured could behave like a dielectric.

5.2 Beam-screen Reflectometry

A huge range of different objects has been tested providing a good overview of the behavior of different shapes and materials. The data collected is compiled into a reference guide, which can be used for comparison purposes. The capability and limits of the system were clearly identified. The size of the reflection depends on many different parameters, like size, shape and especially orientation of the samples. The orientation plays an important rule when one dimension is much larger than the others. Useful correlations could only be made for varying sizes of samples. It was also found that measurements without the protection caps do not have to cope with mode conversion, therefore future measurements will be done without protection caps. The results of the measurements confirm once more the demand for additional visual inspection by endoscopy. Nevertheless the data collected enables future users to obtain a rapid overview of the capability of the system and to learn how to interpret the signals.

6 Acknowledgments

This thesis was accomplished within the framework of the CERN Technical Student Program. I would like to express my gratitude to my supervisor Fritz Caspers for his considerate supervision, many salutary discussions and all the material he placed at my disposal. I have to mention Lloyd Williams as well, as he had countless good ideas and supported my work in many other ways. Another person from whose great experience with the beam-screen reflectometer and a lot of useful inputs I benefited from, is Pawel Borowiec.

Many thanks to Wilhelmus Vollenberg, who patiently taught me lessons about the coating process and did the measured coatings for me. The staff from the workshop supported my work, with various help in constructing the test track, as well.

Special thanks go to my Austrian supervisor Helmut Frais-Kölbl from the University of Applied Sciences Wiener Neustadt, who agreed to supervise me and from whose long experience with CERN-projects I benefited.

Also important to mention is the relaxed and welcoming employee attitude and the hospitality at CERN and therefore, I express many thanks to all the members of my section, including our section leader Jean-Philippe Tock.

Last but not least I want to say thanks to my family and all my friends supporting my stay here in all possible, those to whom this is particularly addressed to, know.

7 List of Abbreviations

LHC	Large Hadron Collider
NEG	Non Evaporable Getter
TDR	Time Domain Reflectometry
RMS	Root Mean Square
DUT	Device Under Test
SNA	Scalar Network analyzer
VNA	Vector Network analyzer
RF	Radio Frequency
CW	Carrier Wave
LO	Local Oscillator
IF	Intermediate Frequency
TEM	Transversal Electro Magnetic
TE	Transversal Electric
TM	Transversal Magnetic
FFT	Fast Fourier Transform
iFFT	inverse Fast Fourier Transform
SNR	Signal to Noise Ratio
SPS	Super Proton Synchrotron
SEY	Secondary Electron Yield
Q-factor	Quality factor
PEC	Perfect Electric Conductor

8 List of Figures

9 List of References

[1]. *NEG Coating @ ELETTRA: 4 years of Experience.* **F. Mazzolini, J.Miertusova, L.Rumiz.** Trieste : ELLETRA, April 5–8 2006.

[2]. *The use of NEG Pumps and Coatings in Large Vacuum Systems:Experience and limitations.* **Mazzolini, Fabio.** Trieste : Elettra, 2006.

[3]. *Impact of NEG Coating on the Impedance.* **Nagaoka, R.** Gif-sur-Yvette : Synchrotron SOLEIL, 2003.

[4]. *STUDY OF RESISTIVE-WALL EFFECTS ON SOLEIL.* **Nagaoka, R.** Gif-sur-Yvette : Synchrotron SOLEIL, 2004.

[5]. *NEG-COATED VACUUM CHAMBERS AT THE ESRF: PRESENT STATUS.* **Kersevan, R.** Grenoble : ESRF, 2002.

[6]. **H. Meinke, F.W. Gundlach.** *Taschenbuch der Hochfrequenztechnik.* Berlin/Heidelberg/New York : Springer Verlag, 1968.

[7]. **Petermann, Prof. Dr. -Ing Klaus.** Hochfrequnztechnik I Vorlesungsskript. s.l. : TU Berlin, 2008.

[8]. *Thin-Film Basics Begin At The Atomic Level.* **Smith, James F.** s.l. : MICROWAVES & RF, December 2008.

[9]. **Maissel, Leon I.** *Handbook of Thin Film Technology.* New York : McGraw-Hill, 1970.

[10]. Picture taken by Author.

[11]. *The secondary electron yield of technical materials nad its variation with surface treatments.* **N.Hilleret.** Geneva : CERN, 2000.

[12]. **Chao, Shuh-Han.** Measurements of Microwave Conductivity and Dielectric Constant by the Cavity Perturbation Method and Their Errors. *IEEE Transactions on Microwave Theory and Techniques.* 1985, Vols. MTT-33.

[13]. **G. Singh, A. Kumar and S. Sharma.** Measurement of Dielectric Constant and Loss Factor of the Dielectric Material at Microwave Frequencies. *Progress In Electromagnetics Research.* 2007, Vol. 69.

[14]. **M. Hajian, K. T. Mathew and L. P. Ligthart.** Measurement of Complex Permittivity with Waveguide Resonator using Perturbation Technique. *MICROWAVE AND OPTICAL TECHNOLOGY LETTERS.* 1999, Vol. 21.

[15]. **Mi Lin, Yong Wang and Mohammed N. Afsar.** *Precision Measurement Of Complex Permittivity And Permeability By Microwave Cavity Perturbation Technique.* Medford : Tufts University.

[16]. **N.Afsar, Mi Lin and Mohammed.** *A new cavity perturbation technique for accurate measurement of dielectric parameters.* Medford : Tufts University.

[17]. **Raveendranath, K.T. Mathew and U.** *Cavity Perturbation Techniques for Measuring Dielectric Parameters of Water and Other Allied Liquids.* Kerala : Cochin University of Science and Technology.

[18]. Private Conversation with Wilhelmus Vollenberg.

[19]. **Gao, J.** Effects of the Cavity Walls on Perturbation Measurements. *IEEE Transactions on Instrumentation and Measurement.* 1991, Vol. 40.

[20]. *Mechanical Design Aspects of the LHC Beam Screen.* **Various.** Geneva : CERN, 1997.

[21]. **Kroyer, T.** *A waveguide High Order Mode Reflectometer for the Large Hadron Collider Beam-pipe.* s.l. : TU Wien, 2003. Dipl. thesis.

[22]. **Kroyer, T.** *Application of Waveguide Diagnostics for Remote Sensing in Accelorator Beam Pipes.* s.l. : TU Wien, 2005. Phd Thesis.

[23]. **F. Caspers, T. Kroyer.** *Coupler Structure for the LHC Beam Pipe Waveguide Mode Reflectometer.* Geneva : CERN, 2004.

[24]. **Prodromides, Alexandra.** *Non-Evaporable Getter Thin Film Coatings for Vacuum Applications.* s.l. : ECOLE POLYTECHNIQUE FÉDÉRALE DE LAUSANNE, 2002.

[25]. **Caspers, F.** *JUAS RF Engineering.* 2009.

[26]. Modified. [Online] http://en.wikipedia.org/wiki/File:Vna3.png.